

## Search for high-mass protostars with ALMA revealed up to kilo-parsec scales (SPARKS)

### II. Complex organic molecules and heavy water in shocks around a young high-mass protostar<sup>★</sup>

T. Csengeri<sup>1,2</sup>, A. Belloche<sup>1</sup>, S. Bontemps<sup>2</sup>, F. Wyrowski<sup>1</sup>, K. M. Menten<sup>1</sup>, and L. Bouscasse<sup>1</sup>

<sup>1</sup> Max Planck Institute for Radioastronomy, Auf dem Hügel 69, 53121 Bonn, Germany  
e-mail: [csengeri@mpifr-bonn.mpg.de](mailto:csengeri@mpifr-bonn.mpg.de)

<sup>2</sup> Laboratoire d'astrophysique de Bordeaux, Univ. Bordeaux, CNRS, B18N, allée Geoffroy Saint-Hilaire, 33615 Pessac, France

Received 7 February 2019 / Accepted 25 September 2019

#### ABSTRACT

**Context.** Classical hot cores are rich in molecular emission, and they show a high abundance of complex organic molecules (COMs). The emergence of molecular complexity that is represented by COMs, in particular, is poorly constrained in the early evolution of hot cores.

**Aims.** We put observational constraints on the physical location of COMs in a resolved high-mass protostellar envelope associated with the G328.2551–0.5321 clump. The protostar is single down to  $\sim 400$  au scales and we resolved the envelope structure down to this scale.

**Methods.** High angular resolution observations using the Atacama Large Millimeter Array allowed us to resolve the structure of the inner envelope and pin down the emission region of COMs. We use local thermodynamic equilibrium modelling of the available 7.5 GHz bandwidth around  $\sim 345$  GHz to identify the COMs towards two accretion shocks and a selected position representing the bulk emission of the inner envelope. We quantitatively discuss the derived molecular column densities and abundances towards these positions, and use our line identification to qualitatively compare this to the emission of COMs seen towards the central position, corresponding to the protostar and its accretion disk.

**Results.** We detect emission from 10 COMs, and identify a line of deuterated water (HDO). In addition to methanol ( $\text{CH}_3\text{OH}$ ), methyl formate ( $\text{CH}_3\text{OCHO}$ ) and formamide ( $\text{HC}(\text{O})\text{NH}_2$ ) have the most extended emission. Together with HDO, these molecules are found to be associated with both the accretion shocks and the inner envelope, which has a moderate temperature of  $T_{\text{kin}} \sim 110$  K. We find a significant difference in the distribution of COMs. O-bearing COMs, such as ethanol, acetone, and ethylene glycol are almost exclusively found and show a higher abundance towards the accretion shocks with  $T_{\text{kin}} \sim 180$  K. Whereas N-bearing COMs with a CN group, such as vinyl and ethyl cyanide peak on the central position, thus the protostar and the accretion disk. The molecular composition is similar towards the two shock positions, while it is significantly different towards the inner envelope, suggesting an increase in abundance of O-bearing COMs towards the accretion shocks.

**Conclusions.** We present the first observational evidence for a large column density of COMs seen towards accretion shocks at the centrifugal barrier at the inner envelope. The overall molecular emission shows increased molecular abundances of COMs towards the accretion shocks compared to the inner envelope. The bulk of the gas from the inner envelope is still at a moderate temperature of  $T_{\text{kin}} \sim 110$  K, and we find that the radiatively heated inner region is very compact ( $< 1000$  au). Since the molecular composition is dominated by that of the accretion shocks and the radiatively heated hot inner region is very compact, we propose this source to be a precursor to a classical, radiatively heated hot core. By imaging the physical location of HDO, we find that it is consistent with an origin within the moderately heated inner envelope, suggesting that it originates from sublimation of ice from the grain surface and its destruction in the vicinity of the heating source has not been efficient yet.

**Key words.** astrochemistry – stars: massive – stars: formation – submillimeter: ISM – ISM: molecules

### 1. Introduction

The origin of complex organic molecules (COMs) that emerge during the process of star and planet formation is a key question in understanding our astrochemical origins. Historically, COMs in the interstellar medium have been identified towards so called hot cores associated with sites of high-mass star formation (Blake et al. 1987; Garay & Lizano 1999; Kurtz et al. 2000). In

these objects, radiative heating from the central protostar leads to an increase in temperature that can reach  $T \gtrsim 100$ –200 K over an extent of 0.05–0.1 pc, leading to a boost of chemical complexity due to thermal desorption of heavier molecules from the ice mantles and grain surfaces, and subsequent gas-phase reactions. As a result, classical hot cores exhibit a high abundance of COMs (e.g. Bisschop et al. 2007; Mookerjea et al. 2007; Beltrán et al. 2009; Widicus Weaver et al. 2017).

The formation of COMs was first modelled by invoking gas-phase chemical reactions (e.g. Millar et al. 1991; Charnley et al. 1992; Caselli et al. 1993); recent chemical models assign,

<sup>★</sup> A copy of the reduced datacubes is available at the CDS via anonymous ftp to [cdsarc.u-strasbg.fr/130.79.128.5](http://cdsarc.u-strasbg.fr/ftp/130.79.128.5) or via <http://cdsarc.u-strasbg.fr/viz-bin/cat/J/A+A/632/A57>

however, an important role to reactions on the grain-surface (Charnley 2001; Garrod & Herbst 2006; Garrod & Widicus Weaver 2013, see however Balucani et al. 2015). According to these models, COMs are thought to form in the ice mantles of interstellar dust grains (Herbst & van Dishoeck 2009). First, through the hydrogenation of atoms and small molecules, the “zeroth-generation” species of small saturated COMs, such as CH<sub>3</sub>OH, form. The diffusion and recombination of these small molecules and radicals lead to the emergence of “first-generation” COMs, which becomes efficient at  $\gtrsim 30$  K (Garrod & Herbst 2006). When the radiative feedback from the emerging protostar heats up its environment to  $\gtrsim 100$  K, molecules sublime from the grains and the “second-generation” COMs form through gas-phase reactions.

This relatively simple picture of hot core formation and chemistry seems to be, however, more complicated because while all hot cores are rich in molecular emission, they exhibit a significant diversity in their chemical composition (Walmsley & Schilke 1993; Kurtz et al. 2000; Churchwell 2002; Bisschop et al. 2007; Calcutt et al. 2014; Widicus Weaver et al. 2017; Bonfand et al. 2017; Sánchez-Monge et al. 2017; Allen et al. 2018). The origin of this diversity is not fully understood. To understand the key processes leading to the formation of COMs, first the physical conditions, in which these molecules appear, need to be constrained. In practice this means determining in which component of the envelope they reside, allowing us to pinpoint whether they originate from the cold or the heated parts of the envelope, or are associated with slow or fast shocks. Constraining the chemical differentiation of the inner envelope observationally is therefore particularly important because resolving the physical location of COMs reveals the physical conditions of the gas, which can help to constrain their chemical formation pathways. This can be used as a tool to investigate both the physical and chemical processes related to star formation and the emergence of molecular complexity (Garrod & Widicus Weaver 2013; Sakai et al. 2014).

Measured with single dish telescopes, incapable of resolving individual massive envelopes, the origin of chemical differentiation is, however, challenging to identify. Reaching the scales of a few hundred au resolution ( $<0.^{\prime}1$  at distances of several kpc) is necessary to resolve the spatial distribution of COMs within high-mass protostellar envelopes. While this information would provide valuable input to constrain chemical models, this is a largely unexplored territory for the precursors of high-mass stars. In the past, due to angular resolution and sensitivity limitations, typically only the brightest hot cores have been studied (e.g. Palau et al. 2011, 2017; Jiménez-Serra et al. 2012; Widicus Weaver & Friedel 2012; Friedel & Widicus Weaver 2012; Öberg et al. 2013; Allen et al. 2017). These are frequently found in regions in which confusion due to the clustered nature of (high-mass) star formation limits the possibility to reveal the spatial location of COMs within single envelopes.

High angular resolution and high sensitivity observations with the Atacama Large Millimeter Array (ALMA) provide now an increasingly rich insight into the close vicinity of forming O-type stars. An emerging number of observational studies show in unprecedented detail the resolved structure of high-mass clusters and protostellar envelopes (Sánchez-Monge et al. 2013; Maud et al. 2017; Ginsburg et al. 2017; Csengeri et al. 2018, hereafter Paper I). Some show an increasing complexity towards smaller scales in terms of clustering, while rare examples of single high-mass protostellar envelopes have been identified (Paper I). Here we study the molecular composition

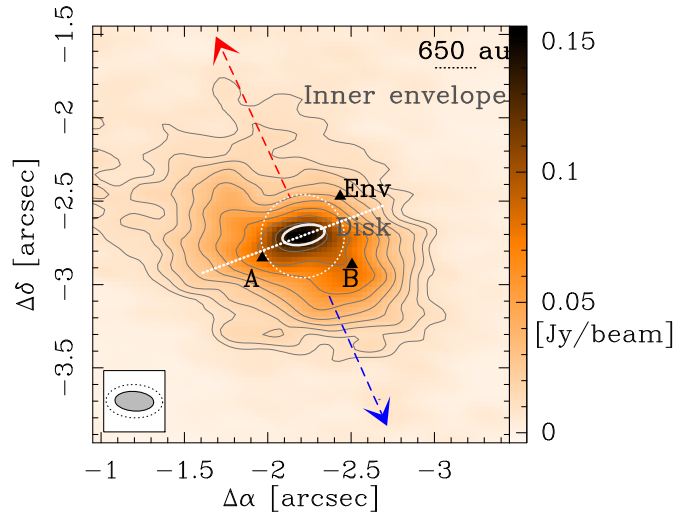


**Fig. 1.** Line-free continuum emission map at 345 GHz combining ALMA 12 m and 7 m arrays from Paper I imaged with robust parameter of  $-2$  giving a beam size with a geometric mean of  $0.^{\prime}16$ . The colour scale is linear between  $-3\sigma$  and  $120\sigma$ , where  $1\sigma$  is  $1.3 \text{ mJy beam}^{-1}$ , contours start at  $7\sigma$  and increase on a logarithmic scale up to  $120\sigma$  by a factor of 1.37. The red and blue dashed lines show the direction of the CO outflow. The dotted line indicates the direction perpendicular to the outflow, and the white ellipse shows the position of the accretion disk from Paper I. The HPBW of the synthesised beam is shown in the lower left corner; the filled ellipse corresponds to that of the continuum image, the dotted ellipse to the molecular line data of this paper. Black triangles mark the positions where the spectra have been extracted for this work, and the white dotted circle shows the area with a radius of  $0.^{\prime}5$  where the spectra have been averaged.

of the gas in the immediate vicinity of G328.2551-0.5321, a hot core precursor, on few hundred au scales. This source is the only massive object embedded in the MSXDC G328.25-00.51 dark cloud that is located at a distance of  $2.5^{+1.7}_{-0.5}$  kpc. It was identified by Csengeri et al. (2017) based on the APEX Telescope Large Area Survey of the Galaxy (ATLASGAL) (Schuller et al. 2009; Csengeri et al. 2014, 2017) at  $870 \mu\text{m}$ , and was observed in the frame of the SPARKS project (Search for High-mass Protostars with ALMA revealed up to kilo-parsec scales, Csengeri et al., in prep.). In Paper I we show that the physical structure of this source is dominated by a single collapsing envelope down to  $\sim 400$  au scales (Fig. 1), which makes it an ideal laboratory to study the emergence of hot cores. We estimate the protostellar mass to be between  $\sim 11$  and  $16 M_{\odot}$  with an envelope mass  $\sim 120 M_{\odot}$  (Paper I). For the first time, we find indication for shocked gas in the 300–800 au vicinity of the protostar that has been identified using a rotational transition of CH<sub>3</sub>OH from within its first torsionally excited state, and is interpreted to outline accretion shocks (Fig. 1, A and B positions, Paper I). This phenomenon has been observed towards nearby low-mass protostars (Sakai et al. 2014; Oya et al. 2017), and is expected to arise due to the infall from the envelope onto a compact, rotationally supported accretion disk. Here we focus on the molecular composition of the observed accretion shocks and reveal spatially resolved emission from several COMs as new tracers pinpointing these shocks.

The paper is organised as follows: in Sect. 2 we present the observations and the data reduction; in Sect. 3 we show the spectra towards the selected positions and analyse their molecular composition. In Sect. 4 we discuss the results, and finally in Sect. 5 we present our conclusions.

## 2. Observations and data reduction

The observations have been carried out with ALMA in Cycle 2 using 35 of the 12 m antennas on 2015 May 3, and 2015 September 1. The phase centre was  $(\alpha, \delta)_{2000} = (15^{\text{h}}58^{\text{m}}00.05^{\text{s}}, -53^{\circ}57'57.8'')$  and the baseline range is 15 m (17  $\text{k}\lambda$ ) to 1574 m (1809  $\text{k}\lambda$ ). The total time on source was 7.4 min, and the  $T_{\text{sys}}$  varies between 120 and 200 K. The calibrators have been J1517–2422 (bandpass), J1617–5848 (phase) and the absolute flux scale has been calibrated based on observations of Titan and Ceres. The atmospheric conditions have been stable over both measurement sets with a precipitable water vapour of  $\sim 0.8$  and  $\sim 1.1$  mm for the more extended and the compact configuration, respectively. We estimate an absolute flux uncertainty around  $\sim 10\%$  by comparing the measured and catalogue fluxes for the two measurement sets for the bandpass and phase calibrators. The bandpass calibrator was measured less frequently and shows on average larger flux variations over the timescale of the two measurement sets compared to the phase calibrator, which does not show strong flux variations over this period. Here we measure a maximum discrepancy between the catalogue and the measured value up to 12%. We used four basebands in Band 7 centred on 347.331, 345.796, 337.061, and 333.900 GHz, respectively. This gives a  $4 \times 1.75$  GHz effective bandwidth with a spectral resolution of 0.977 MHz corresponding to  $\sim 0.9 \text{ km s}^{-1}$  velocity resolution.

The data have been calibrated in CASA 4.3.1 with the pipeline (version 34.044). We imaged and cleaned the data using Briggs weighting and used the CLEAN algorithm for deconvolution. In this work we used a robust parameter of 0.5 for the imaging<sup>1</sup> to favour sensitivity.

We first created a cube of the entire bandwidth with a synthesised half-power beam width (HPBW) of  $0.^{\prime}30 \times 0.^{\prime}17$  and a position angle of 88.37 degrees. The geometric mean of the major and minor axes corresponds to a beam size of  $0.^{\prime\prime}23$  ( $\sim 575$  au). We then extracted spectra of the entire frequency coverage towards representative positions corresponding to the two accretion shock spots, and a position representing the inner envelope (Fig. 1). The spectra were then exported to GILDAS/CLASS<sup>2</sup> for further processing. We subtracted the continuum emission from these spectra by selecting line emission free channels, and using a zero order baseline. To convert the spectra from Jy beam<sup>-1</sup> to Kelvin units we used a factor of 198 based on the geometric mean of the synthesized HPBW.

We also show here images of molecular line emission, where we imaged a narrow velocity range around the selected line. In an iterative process, we first created the image, then identified the emission free channels towards the continuum peak and close to the selected line emission. We then subtracted the continuum emission in the *uv*-data, performed the gridding and the deconvolution procedure, as described above, to obtain continuum free data cubes around a list of selected lines.

We only focus here on molecular emission that originates from scales typically smaller than the largest angular scales of  $\sim 7''$ , beyond which the sensitivity of our 12 m array observations drops. We have therefore not used information from the more compact 7 m array. We measure a  $1\sigma$  rms noise level of  $\sim 3$  K in brightness temperature ( $T_b$ ) scales in a spectral resolution of

0.977 MHz. The spectral setup and data reduction for our target is described in more details in Paper I.

## 3. Results and analysis

We investigate here the physical properties of the gas and aim to explore its molecular composition with a particular focus on COMs within this high-mass protostellar envelope. In Fig. 2, we show the spectrum towards the central position averaged within a radius of  $0.^{\prime\prime}5$  (Fig. 1), and as a comparison the spectrum extracted towards the accretion shock position labelled as  $B$ , and the central position corresponding to the protostar and its accretion disk. It is clear that the gas is rich in molecular emission, and we identify and list the brightest transitions of simple molecules in Table 1.

We present a quantitative analysis towards three positions corresponding to the two locations of accretion shocks (one of them shown in Fig. 2), and the bulk of the inner envelope represented by a position offset from both the accretion shocks and the outflow impacted gas (Fig. 1). The severe blending due to the larger line-widths and the significant uncertainty of dust temperature and opacity hinders us from a quantitative analysis of the spectrum towards the central position, nevertheless, we show and qualitatively discuss its molecular emission corresponding to the protostar and its accretion disk. We show the extracted spectrum towards the  $B$ -shock position with the brightest emission lines, and hence the richest spectrum in detail in Fig. 3 covering a 7.5 GHz bandwidth where we also label unblended transitions of the identified COMs. The same figure for the other positions, corresponding to the  $A$ -shock position and the position representing the bulk emission of the inner envelope, are shown in Appendix A.

### 3.1. Line fitting and LTE modelling

Since the volume density in the inner envelope is expected to be high ( $\bar{n} \gtrsim 10^7 \text{ cm}^{-3}$ , Paper I), we model the spectra assuming that local thermodynamic equilibrium (LTE) conditions apply. We used the Weeds package (Maret et al. 2011), and fitted the spectra in an iterative process. Corrections for the torsionally and vibrationally excited states' contribution to the rotational partition function, and thus to the column density, were derived for the main isotopologue of the listed species.

The steps of the fitting are the following. We first determined the molecular column density ( $N$ ) and the kinetic temperature ( $T_{\text{kin}}$ ) of CH<sub>3</sub>OH. For this the input parameters are  $N(\text{CH}_3\text{OH})$ ,  $T_{\text{kin}}$ , source size, rest velocity ( $v_{\text{lsr}}$ ) and linewidth ( $\Delta v$ ). We fixed the source size to  $0.^{\prime\prime}4$  which is larger than the beam. While emission for the modelled transitions may have different source sizes, as long as they are spatially resolved, the actual source size does not significantly influence the result. Later, from Fig. 4, it is clear that this assumption holds, although emission from the  $B$ -shock position seems to be more compact compared to the other positions. Overestimating the source size would lead to an underestimation of the molecular column densities. The  $v_{\text{lsr}}$  and  $\Delta v$  are measured using a Gaussian fit to the CH<sub>3</sub>OH lines and these values are reported in Paper I. We also considered the continuum emission in our models that we have directly extracted from the fitted baseline of the spectra. These parameters, together with the position, the measured continuum flux density, and the results of the two free parameters,  $N(\text{CH}_3\text{OH})$  and  $T_{\text{kin}}$  are summarised in Table 2.

To constrain  $N(\text{CH}_3\text{OH})$  and  $T_{\text{kin}}$ , we created a grid of models exploring a parameter range of  $N(\text{CH}_3\text{OH}) = 10^{17} \text{--} 10^{20} \text{ cm}^{-2}$

<sup>1</sup> For the line-free continuum maps presented in Paper I we used a robust parameter of  $-2$  to give more weight to the longer baselines yielding a better angular resolution of  $0.^{\prime}16$  corresponding to  $\sim 400$  au physical scales.

<sup>2</sup> [https://www.iram.fr/IRAMFR/GILDAS/](http://www.iram.fr/IRAMFR/GILDAS/)

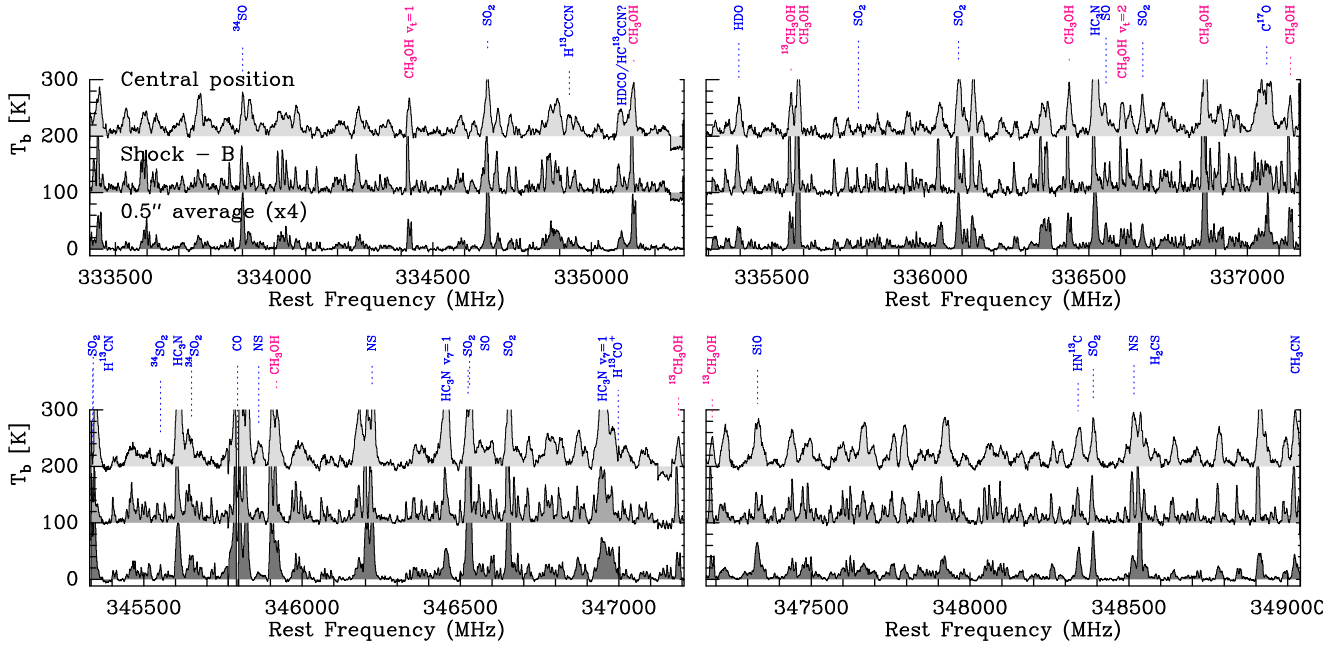


**Fig. 2.** Grey filled histograms show spectra converted to brightness temperature ( $T_b$ ) scale: spectrum extracted towards the central position, the  $B$ -shock position, and an average within a radius of  $0.5''$  around the peak of the dust continuum emission, which is multiplied by a factor of 4 for a better visibility. The blue labels show the species listed in Table 1, pink labels show transitions of  $\text{CH}_3\text{OH}$  (and its isotopologue) discussed in Paper I. The spectra have been shifted along the  $y$ -axis for a better visibility.

and  $T_{\text{kin}} = 50\text{--}300\text{ K}$ . To select the best fit, we computed the residuals of each fit, and visually inspected the results with a particular emphasis on the optically thin lines and the unblended transitions of  $\text{CH}_3\text{OH}$  listed in Table 1. The resulting  $T_{\text{kin}}$  was then used to estimate  $N_{\text{H}_2}$  based on the dust continuum emission assuming that the gas and the dust are thermalised at these high densities, hence  $T_d = T_{\text{kin}}$ . For this we used  $N(\text{H}_2) = \frac{F_\nu R}{B_\nu(T_d) \Omega \kappa_\nu \mu_{\text{H}_2} m_{\text{H}}} [\text{cm}^{-2}]$ , where  $F_\nu$  is the beam averaged flux density towards the selected positions,  $B_\nu(T)$  is the Planck function,  $\Omega$  is the solid angle of the beam calculated by  $\Omega = 1.13 \times \Theta^2$ , where  $\Theta$  is the geometric mean of the beam major and minor axes;  $\kappa_\nu = 0.0185 \text{ cm}^2 \text{ g}^{-1}$  from Ossenkopf & Henning (1994) at 345 GHz including the gas-to-dust ratio,  $R$ , of 100;  $\mu_{\text{H}_2}$  is the mean molecular weight per hydrogen molecule and is equal to 2.8; and  $m_{\text{H}}$  is the mass of a hydrogen atom.

We find that the derived parameters are similar for the two shock positions, the  $\text{CH}_3\text{OH}$  column density reaches up to  $2 \times 10^{19} \text{ cm}^{-2}$ , and the kinetic temperature is around 180 K. As pointed out in Paper I, temperatures above  $\sim 200$  K are not consistent with the observations because other  $\text{CH}_3\text{OH}$  lines would appear brighter than the emission seen at the corresponding frequencies. Towards the position of the inner envelope, our models suggest a factor of 5 lower  $\text{CH}_3\text{OH}$  column density, and a considerably lower kinetic temperature of 110 K. In Table 2 we give the range of values that are consistent with the data within  $3\sigma$ , and mark in bold the best fit value adopted for the following modelling.

After fitting the  $\text{CH}_3\text{OH}$  transitions, we created the models for other molecules using the same parameters ( $v_{\text{lsr}}$ ,  $\Delta v$ ,  $T_{\text{kin}}$  and source size) as for  $\text{CH}_3\text{OH}$  using the CDMS (Müller et al. 2005; Endres et al. 2016) and JPL (Pickett et al. 1998) molecular databases. Varying the molecular column density (relative to methanol) we fitted the brightest unblended transitions of each species and visually inspected the result. As shown later in Fig. 4, the adopted source size corresponding to spatially

resolved emission holds for most of the molecules, however, some of the highest energy transitions seem to originate from a more compact region which we do not account for in our model. As a consequence, the column densities for these molecules may be underestimated. As our composite final model shows, these parameters give a good agreement with the spectra. The line-width of vinyl and ethyl cyanide are, however, larger than that of methanol with line-widths up to  $8 \text{ km s}^{-1}$ . Such a larger value would lead to molecular column densities up to 50% higher than the value given by our model.

We obtained the final model in an iterative process, by first fitting the brightest emission of a new species independently, and then visually inspected the full model including all identified species and checked whether the overall fit result remains reasonably good. This is necessary due to the large fraction of blended transitions. Subsequently, once a molecule was identified, we included its isotopologue in the model, and searched for rotational transitions of their lowest energy vibrationally excited states. However, except for  $\text{CH}_3\text{OH}$   $v_t = 1$  and  $\text{HC}_3\text{N}$   $v_7 = 1$ , we have no clear detection of emission from such higher energy, vibrationally excited states.

Altogether we could identify emission from 10 COMs in the spectra. We list the results of the fit, such as their relative fraction compared to  $\text{CH}_3\text{OH}$ , molecular column density, and abundance in Table 4 for the three positions. We show the spectrum for the  $B$ -shock position and the best-fit model in Fig. 3, where we label the least blended lines of each molecule.

### 3.2. Detection of COMs

While the available, non continuous 7.5 GHz bandwidth offers limited spectral coverage to perform a complete analysis of all the molecules that have lines in the spectra, we are able to identify several transitions from ten COMs (Table 3). This frequency range covers transitions over a broad range of upper energy levels

**Table 1.** Summary of detected simple molecules and their transitions.

| Molecule                                  | Transition                             | Frequency<br>[GHz]     | $E_{\text{up}}/k$<br>[K] | Database |
|---|--|------------------------|--------------------------|----------|
| $^{34}\text{SO}$                          | 7 <sub>8</sub> –6 <sub>7</sub>         | 333.901                | 80                       | CDMS     |
| $\text{SO}_2$                             | 8 <sub>2,6</sub> –7 <sub>1,7</sub>     | 334.673                | 43                       | CDMS     |
| $\text{H}^{13}\text{CCCN}$                | 38–37                                  | 334.930                | 314                      | CDMS     |
| $\text{HC}^{13}\text{CCN}$ <sup>(?)</sup> | 37–36                                  | 335.093                | 305                      | CDMS     |
| $\text{HDCO}$ <sup>(?)</sup>              | 5 <sub>1,4</sub> –4 <sub>1,3</sub>     | 335.097                | 56                       | CDMS     |
| $\text{HDO}$                              | 3 <sub>3,1</sub> –4 <sub>2,2</sub>     | 335.396                | 335                      | JPL      |
| $\text{SO}_2$                             | 29 <sub>5,25</sub> –30 <sub>2,28</sub> | 335.773                | 463                      | CDMS     |
| $\text{SO}_2$                             | 23 <sub>3,21</sub> –23 <sub>2,22</sub> | 336.089                | 276                      | CDMS     |
| $\text{HC}_3\text{N}$                     | 37–36                                  | 336.521                | 307                      | CDMS     |
| $\text{SO}$                               | 10 <sub>11</sub> –10 <sub>10</sub>     | 336.554                | 143                      | CDMS     |
| $\text{SO}_2$                             | 16 <sub>7,9</sub> –17 <sub>6,12</sub>  | 336.670                | 245                      | CDMS     |
| $\text{C}^{17}\text{O}$                   | 3–2                                    | 337.061 <sup>(a)</sup> | 32                       | CDMS     |
| $\text{SO}_2$                             | 13 <sub>2,12</sub> –12 <sub>1,11</sub> | 345.339                | 93                       | CDMS     |
| $\text{H}^{13}\text{CN}$                  | 4–3                                    | 345.340                | 41                       | CDMS     |
| $^{34}\text{SO}_2$                        | 6 <sub>4,2</sub> –6 <sub>3,3</sub>     | 345.553                | 57                       | CDMS     |
| $\text{HC}_3\text{N}$                     | 38–37                                  | 345.609                | 324                      | CDMS     |
| $^{34}\text{SO}_2$                        | 5 <sub>4,2</sub> –5 <sub>3,3</sub>     | 345.651                | 51                       | CDMS     |
| $\text{CO}$                               | 3–2                                    | 345.796                | 33                       | CDMS     |
| $\text{NS } \Omega = 1/2, l = e$          | 15/2–13/2                              | 345.823 <sup>(b)</sup> | 70                       | CDMS     |
| $\text{NS } \Omega = 1/2, l = f$          | 15/2–13/2                              | 346.221 <sup>(c)</sup> | 70                       | CDMS     |
| $\text{HC}_3\text{N}, v_7 = 1, l = 1e$    | 38–37                                  | 346.456                | 645                      | CDMS     |
| $\text{SO}_2$                             | 16 <sub>4,12</sub> –16 <sub>3,13</sub> | 346.524                | 165                      | CDMS     |
| $\text{SO}$                               | 9 <sub>8</sub> –8 <sub>7</sub>         | 346.529                | 79                       | CDMS     |
| $\text{SO}_2$                             | 19 <sub>1,19</sub> –18 <sub>0,18</sub> | 346.652                | 168                      | CDMS     |
| $\text{HC}_3\text{N}, v_7 = 1, l = 1f$    | 38–37                                  | 346.949                | 646                      | CDMS     |
| $\text{H}^{13}\text{CO}^+$                | 4–3                                    | 346.998                | 42                       | CDMS     |
| $\text{SiO}$                              | 8–7                                    | 347.331                | 75                       | CDMS     |
| $\text{HN}^{13}\text{C}$                  | 4–3                                    | 348.340                | 42                       | CDMS     |
| $\text{SO}_2$                             | 24 <sub>2,22</sub> –23 <sub>3,21</sub> | 348.388                | 292                      | CDMS     |
| $\text{NS } \Omega = 3/2$                 | 15/2–13/2                              | 348.516 <sup>(c)</sup> | 390                      | CDMS     |
| $\text{H}_2\text{CS}$                     | 10 <sub>1,9</sub> –9 <sub>1,8</sub>    | 348.534                | 105                      | CDMS     |
| $\text{CH}_3\text{CN}$                    | 19–18, K = 8 <sup>(d)</sup>            | 349.025                | 624                      | CDMS     |
| $\text{CH}_3\text{OH}-A$ $v_t = 0$        | 2 <sub>2</sub> –3 <sub>-1</sub>        | 335.134                | 45                       | CDMS     |
| $\text{CH}_3\text{OH}-A$ $v_t = 0$        | 7 <sub>1</sub> –6 <sub>1</sub>         | 335.582                | 79                       | CDMS     |
| $\text{CH}_3\text{OH}-A$ $v_t = 0$        | 14 <sub>7</sub> –15 <sub>6</sub>       | 336.438                | 488                      | CDMS     |
| $\text{CH}_3\text{OH}-A$ $v_t = 0$        | 12 <sub>-1</sub> –12 <sub>0</sub>      | 336.865                | 197                      | CDMS     |
| $\text{CH}_3\text{OH}-E$ $v_t = 0$        | 3 <sub>3</sub> –4 <sub>2</sub>         | 337.136                | 62                       | CDMS     |
| $\text{CH}_3\text{OH}-E$ $v_t = 1$        | 3 <sub>0</sub> –2 <sub>1</sub>         | 334.427                | 315                      | CDMS     |
| $\text{CH}_3\text{OH}-A$ $v_t = 2$        | 7 <sub>1</sub> –6 <sub>1</sub>         | 336.606                | 747                      | JPL      |
| $^{13}\text{CH}_3\text{OH}-A$ $v_t = 0$   | 12 <sub>-1</sub> –12 <sub>0</sub>      | 335.560                | 193                      | CDMS     |
| $^{13}\text{CH}_3\text{OH}-A$ $v_t = 0$   | 14 <sub>-1</sub> –14 <sub>0</sub>      | 347.188                | 254                      | CDMS     |

**Notes.** <sup>(a)</sup>The frequency corresponds to the  $F = 1/2$ – $3/2$  transition. <sup>(b)</sup>The frequency corresponds to the  $F = 17/2$ – $15/2$  transition. <sup>(c)</sup>The frequency corresponds to the  $F = 15/2$ – $13/2$  and  $F = 13/2$ – $11/2$  transitions. <sup>(d)</sup>The K = 9 transition at 348.911 GHz is likely to be detected, although it is blended with a  $\text{CH}_3\text{OCHO}$  line. <sup>(?)</sup>The “?” mark indicates uncertain line identification due to blending.

( $E_{\text{up}}/k$ ) with a spontaneous decay rate (Einstein A-coefficient) above  $10^{-4}$  s<sup>-1</sup> for all species. The range of upper energy levels is, however, much narrower for the detected transitions and covers a range typically around 150–400 K. Many of these transitions are, however strongly blended in the spectra. The smallest energy range covered is for methyl formate and formamide.

In addition to several methanol (and isotopologue) lines, we detect emission from various O-bearing COMs, such as methyl formate ( $\text{CH}_3\text{OCHO}$   $v = 0$ ), ethanol ( $\text{C}_2\text{H}_5\text{OH}$   $v = 0$ ), acetone ( $\text{CH}_3\text{COCH}_3$   $v = 0$ ), ethylene glycol ( $a(\text{CH}_2\text{OH})_2$ ), and acetaldehyde ( $\text{CH}_3\text{CHO}$ ,  $v = 0$ ). Comparing this list of O-bearing COMs with the typical molecules identified towards hot cores, a notable non detection is dimethyl ether ( $\text{CH}_3\text{OCH}_3$ ) which is often found to be co-existing and spatially correlated with methyl formate (e.g. Brouillet et al. 2013; Jaber et al. 2014) suggesting that they are chemically related (Garrod et al. 2008). The upper limit on its molecular column density suggests, however, that a significant amount of dimethyl ether could remain undetected in this frequency range (see Sect. 4.2).

Among the detected species except methanol, methyl formate has the largest column density up to  $N(\text{CH}_3\text{OCHO}) = 1.0 \times 10^{18}$  cm<sup>-2</sup> corresponding to a relative fraction of 0.05 compared to  $\text{CH}_3\text{OH}$ . The largest number of transitions falling in this band are from acetone, ethylene glycol and acetaldehyde which produce a weed-like spread of spectral lines. Therefore, due to blending and uncertainties in the spectroscopic parameters at such relatively high energy and frequency (Ordu et al. 2019), the identification of these molecules is less robust. As a consequence, and also considering their large fraction of blended transitions, the estimated column density is less robust compared to the other species. In particular, blending seems to be more prevalent for acetone, ethanol and acetaldehyde transitions in the higher frequency spectral windows between 345 and 349 GHz.

We also likely detect formic acid,  $t$ -HCOOH, however, there are only two detectable lines of this molecule falling in our frequency coverage and only one of them is unblended<sup>3</sup>. Our modelling suggests that  $t$ -HCOOH is among the lowest abundance O-bearing COMs, with typically more than two orders of magnitude lower abundance compared to that of  $\text{CH}_3\text{OH}$ .

We also identify N-bearing COMs, such as vinyl cyanide ( $\text{C}_2\text{H}_3\text{CN}$ ), and ethyl cyanide, ( $\text{C}_2\text{H}_5\text{CN}$ ), methyl isocyanate ( $\text{CH}_3\text{NCO}$ ) as well as formamide ( $\text{HC(O)NH}_2$ ). The identification of formamide is, however, less robust since it has practically only one detectable transition that is not blended with other lines in the observed frequency range. Since the unblended formamide line is strong, in order to increase the number of its detectable transitions, we searched for its  $^{13}\text{C}$  isotopologue both in the spectra extracted towards the shock spots and the brightest central position. The brightest isotopologue line ( $J = 16_{2,15}$ – $15_{2,14}$ ) is, however, blended at the frequency of 335.405 GHz, and has a predicted peak line temperature close to the noise level assuming an isotopic ratio of 60 and optically thin emission.

Comparing the molecular abundances between O- and N-bearing COMs, we find more than one order of magnitude lower column densities for the N-bearing COMs, such as vinyl and ethyl cyanide, as well as formamide compared to the O-bearing COMs. O-bearing COMs originating from a colder gas component have been seen on similar scales towards the Orion Hot Core and the Compact Ridge (Caselli et al. 1993), and on somewhat larger scales towards classical hot cores (Qin et al. 2010; Widicus Weaver et al. 2017). However, our analysis in Sect. 3.3 suggests that our initial assumption that all COMs originate from gas with the same physical conditions (i.e.  $T_{\text{kin}}$ ), may not hold, in particular for the central position where COMs with a CN group seem to be more compact with a different spatial origin. In this case our estimation of the column density, especially for  $\text{C}_2\text{H}_3\text{CN}$  and  $\text{C}_2\text{H}_5\text{CN}$  may not be accurate.

<sup>3</sup> The  $^{13}\text{C}$  isotopologue of formic acid has an expected peak line temperature comparable to the noise level.

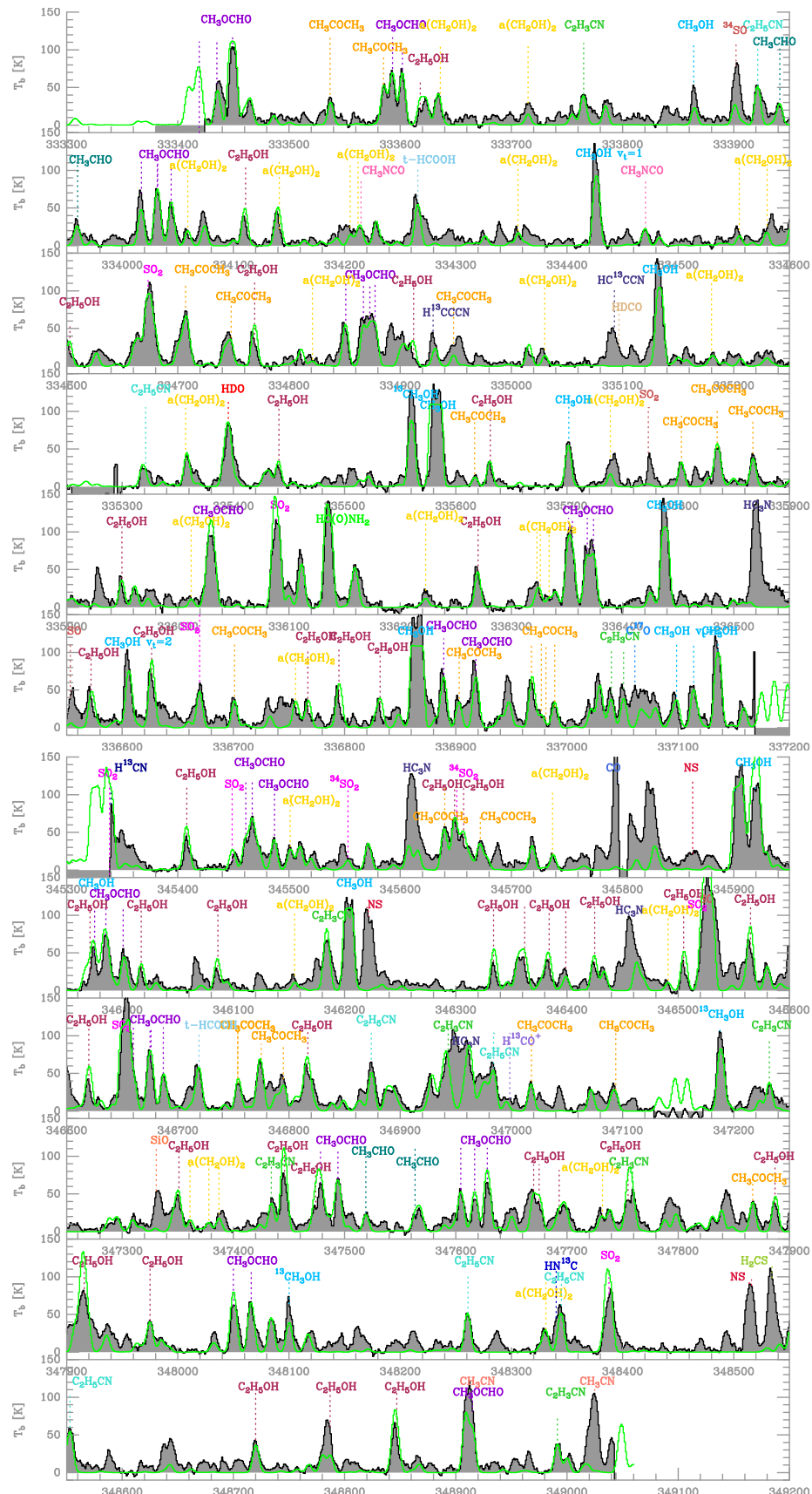


**Fig. 3.** Spectrum extracted towards the *B*-shock position from Paper I. Grey filled histogram shows the observed spectrum converted to brightness temperature ( $T_b$ ) scale, green line shows the composite LTE model including the species listed in Table 3. Coloured labels indicate the least blended transitions of the modelled COMs, as well as other species identified in the spectrum (Table 1). Each colour represents a different molecule and includes its isotopologues as well.

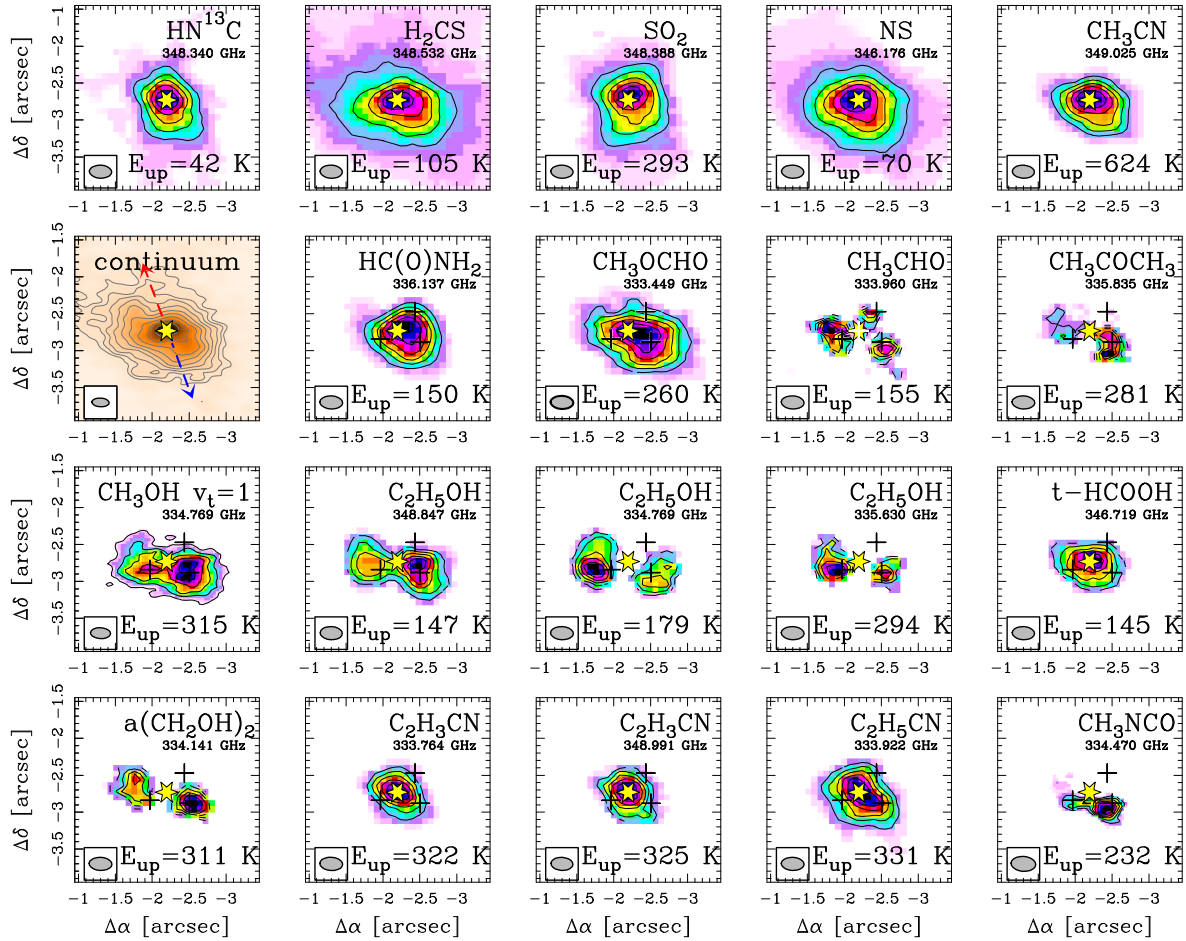


**Fig. 4.** Zeroth moment maps of some simple molecules, and selected transitions of COMs. All contours correspond to significant emission and start at 20% of the maximum value and increase by 15% of the maximum value. Yellow star marks the position of the dust continuum peak corresponding to the central protostar. The beam is shown in the lower left corner. Labels indicate the shown molecular species. One figure shows the continuum as a reference, where the scale and contours are the same as in Fig. 1.

**Table 2.** Positions, their observed 345 GHz continuum emission and modelled methanol parameters.

| Position         | Offset <sup>(a)</sup> | $F_\nu$ <sup>(b)</sup><br>[mJy/beam] | $T_{\text{cont}}$ <sup>(c)</sup><br>[K] | $N(\text{CH}_3\text{OH})$ <sup>(†)</sup><br>[cm <sup>-2</sup> ] | $T_{\text{kin}}$ <sup>(d),(†)</sup><br>[K] | $N_{\text{H}_2}$<br>[cm <sup>-2</sup> ]   |
|------------------|-----------------------|--------------------------------------|---|---|--|---|
| Shock A          | [−1''.96; −2''.85]    | 156                                  | 30.9                                    | $1.2 \times 10^{19} - \mathbf{1.6 \times 10^{19}}$              | 170–190 (180)                              | $2.04 \times 10^{24}$                     |
| Shock B          | [−2''.50; −2''.88]    | 144                                  | 28.5                                    | $1.6 \times 10^{19} - 2.4 \times 10^{19} (2 \times 10^{19})$    | 170–200 (180)                              | $1.89 \times 10^{24}$                     |
| Inner envelope   | [−2''.43; −2''.47]    | 86                                   | 17.0                                    | $\mathbf{4.1 \times 10^{18}} - 8.1 \times 10^{18}$              | 90–110                                     | $1.90 \times 10^{24}$                     |
| Protostar + disk | [−2''.17; −2''.76]    | 239                                  | 47.3                                    |   | 200 – 500                                  | $1.1 - 2.8 \times 10^{24}$ <sup>(e)</sup> |

**Notes.** <sup>(†)</sup>Bold face shows the values from the best fit models. <sup>(a)</sup>The position of the dust continuum peak is at [−2''.17; −2''.76] relative to the phase centre position given in Sect. 2. <sup>(b)</sup>Measured in the synthesized beam of 0''.3 × 0''.17. <sup>(c)</sup>Brightness temperature of the continuum emission on the Rayleigh-Jeans scale. <sup>(d)</sup> $T_{\text{kin}}$  corresponds to the gas temperature estimated from the CH<sub>3</sub>OH lines (Sect. 3.1). <sup>(e)</sup>Neglecting the effect of optical depth.

### 3.3. Spatial distribution of various molecules

Investigating the spatial distribution of the identified molecules, we find a strong chemical differentiation within this high-mass envelope. We show zeroth moment maps calculated over a velocity range of −55 to −35 km s<sup>−1</sup> for some unblended transitions of COMs in Fig. 4, and for comparison, we also show some of the brightest emission from other molecules, such as HN<sup>13</sup>C ( $J = 4-3$ ,  $E_{\text{up}}/k = 42$  K), H<sub>2</sub>CS ( $J = 10 - 1, 9 - 9_{1,8}$ ,  $E_{\text{up}}/k = 105$  K), SO<sub>2</sub> ( $J = 24_{2,22} - 23_{3,21}$ ,  $E_{\text{up}}/k = 293$  K),

NS ( $J = 8_{1,8,7} - 7_{-1,7,6}$ ,  $J = 8_{1,8,8} - 7_{-1,7,7}$ ,  $E_{\text{up}}/k = 70$  K), as well as the  $K = 8-8$  line of the  $J = 19-18$  transition of CH<sub>3</sub>CN ( $E_{\text{up}}/k = 624$  K). All these transitions of simple molecules show the brightest emission towards the peak position of the dust continuum, and show considerably more extended emission towards the inner envelope than the majority of the COMs. Only the shown CH<sub>3</sub>CN line appears relatively compact highlighting the potentially warmer regions in the immediate vicinity of the protostellar embryo.

**Table 3.** Summary of the detected interstellar COMs towards the selected positions.

| Molecule   |                   | $E_{\text{up}}/k$ <sup>(a)</sup><br>(K) | Detected $E_{\text{up}}/k$<br>(K) | Database | Component <sup>(b)</sup> |
|--|-------------------|---|-----------------------------------|----------|--------------------------|
| CH <sub>3</sub> OH                               | Methanol          | 45–1677                                 | 45–488                            | JPL      | e,s                      |
| CH <sub>3</sub> OCHO                             | Methyl formate    | 80–352                                  | 80–352                            | JPL      | e,s                      |
| C <sub>2</sub> H <sub>5</sub> OH                 | Ethanol           | 88–3294                                 | 90–407                            | CDMS     | s                        |
| CH <sub>3</sub> COCH <sub>3</sub> <sup>(c)</sup> | Acetone           | 98–2241                                 | 98–304                            | JPL      | s                        |
| a(CH <sub>2</sub> OH) <sub>2</sub>               | Ethylene glycol   | 98–1729                                 | 266–455                           | CDMS     | s                        |
| CH <sub>3</sub> CHO                              | Acetaldehyde      | 153–807                                 | 153–383                           | JPL      | s                        |
| CH <sub>3</sub> NCO                              | Methyl isocyanate | 323–465                                 | 365–460                           | CDMS     | s                        |
| C <sub>2</sub> H <sub>3</sub> CN                 | Vinyl cyanide     | 300–2531                                | 308–326                           | CDMS     | c                        |
| C <sub>2</sub> H <sub>5</sub> CN                 | Ethyl cyanide     | 60–2032                                 | 72–351                            | CDMS     | c                        |
| HC(O)NH <sub>2</sub> <sup>(d)</sup>              | Formamide         | 136–152                                 | 136–152                           | CDMS     | e,s,c                    |
| <i>t</i> -HCOOH <sup>(d),(e)</sup>               | Formic acid       | 136–645                                 | 145                               | CDMS     | e                        |

**Notes.** <sup>(a)</sup>Range of upper energy levels of all transitions in our frequency coverage with an  $A_{ij}$  above  $10^{-4} \text{ s}^{-1}$ , except for methanol and methyl formate, where the lowest energy transition detected has an  $A_{ij}$  of  $9.87 \times 10^{-5} \text{ s}^{-1}$  and  $2.68 \times 10^{-5} \text{ s}^{-1}$ , respectively. <sup>(b)</sup>The label e corresponds to the inner envelope, s to the accretion shocks, and c to the innermost central regions that could have contribution from both the outflow and the accretion disk. <sup>(c)</sup>Spectroscopic parameters are more uncertain at this frequency range (Ordu et al. 2019). <sup>(d)</sup>The identification is based on only one to two unblended transitions. <sup>(e)</sup>Formic acid contains less than 6 atoms, it is, however, the simplest organic acid and thus will be discussed together with the listed interstellar COMs.

The emission from COMs is rather compact, but typically spatially resolved. Methyl formate shows the most extended morphology coinciding with the highest column density dust emission, however, formamide is also considerably extended. Using a 2D Gaussian fit to the 0th moment map shown in Fig. 4, we measure the beam convolved full-width at half-maximum (FWHM) extent of methyl formate to be  $0.^{\circ}95 \times 0.^{\circ}58$ , corresponding to a beam deconvolved geometric mean of  $0.^{\circ}70$ . Following the formulation in Paper I, we estimate a radius ( $R_{90\%}$ ) of  $0.^{\circ}58$  corresponding to a size of 1450 au. For formamide, we measure a beam convolved FWHM of  $0.^{\circ}62 \times 0.^{\circ}61$ , corresponding to a beam deconvolved geometric mean of  $0.^{\circ}57$ . Similarly as above, this corresponds to a radius of  $0.^{\circ}47$  that is 1175 au.

Qualitatively comparing the emission from the central position towards that of the envelope, it is apparent that the O- versus N-bearing COMs show a striking difference in their morphology; while O-bearing COMs peak offset from the central protostar, N-bearing COMs with a CN group are the brightest towards the central position, thus the protostar and the disk, and show an elongation in the direction of the outflow axis. The most striking example of this dichotomy is seen in ethanol, acetone, acetaldehyde and ethylene glycol versus vinyl and ethyl cyanides. The similar upper energy levels ( $E_{\text{up}}/k = 150–300 \text{ K}$ ) of these transitions (Fig. 4) suggests that the spatial morphology corresponds to genuine chemical differentiation rather than temperature gradients and excitation effects. Similarly as above, using a 2D Gaussian fit, we measure a beam convolved FWHM of the most compact emission of the 348.991 GHz C<sub>2</sub>H<sub>3</sub>CN line of  $0.^{\circ}63 \times 0.^{\circ}51$ , corresponding to a beam deconvolved size of  $0.^{\circ}55 \times 0.^{\circ}47$ . The most compact component of this emission corresponds to an  $R_{90\%}$  radius of  $\sim 900$  au.

The other striking feature is that, all the other typical O-bearing COMs, such as ethanol, acetone, ethylene glycol peak on and only show emission towards the shock positions. The lack of detection of these molecules towards the inner envelope may be, however, due to observational limitation, because the unblended transitions in our frequency coverage are typically above  $E_{\text{up}}/k > 200 \text{ K}$ , hence a combination of sensitivity,

blending and excitation effects may make it difficult to detect these molecules in the relatively colder gas component with  $T_{\text{kin}} \lesssim 100 \text{ K}$ .

### 3.4. Detection and distribution of HDO

The LTE modelling allows us to identify the  $J = 3_{3,1} - 4_{2,2}$  transition of HDO at 335.396 GHz ( $E_{\text{up}}/k = 335 \text{ K}$ ), and requires a high column density of  $2.1–4.0 \times 10^{17} \text{ cm}^{-2}$  to fit the observed line intensity. Our models suggest that this transition is blended with a line of ethylene glycol at 335.397 GHz. In addition, shifted by a few  $\text{km s}^{-1}$  at 335.403 GHz, there is also a methyl formate line which may also show a small contribution to the observed emission at the frequency of the HDO line. However, there is no model that could reproduce the observed spectrum using only ethylene glycol and methyl formate. Our best fit model towards all three position requires including a significant amount of HDO to reproduce the observed line intensity. The spatial extent of the HDO line is comparable to that of methyl formate and formamide, while ethylene glycol for example has a considerably more compact morphology peaking on the accretion shocks. The modelled lines do not contribute to more than 15–21% of the velocity integrated line intensity on the selected positions, therefore we assign the observed emission to the HDO line.

The distribution of the HDO emission together with its velocity field is shown in Fig. 5. It shows an increased intensity towards one of the shock positions, however, its emission is dominated by the inner envelope component showing an extended morphology. The estimated HDO abundance is between  $1.1 \times 10^{-7}$  and  $2.1 \times 10^{-7}$  for all three positions, and is therefore similar towards the shock positions and the inner envelope. Using a 2D Gaussian fit we measure its beam convolved FWHM to be  $\sim 0.^{\circ}86 \times 0.^{\circ}54$  with a deconvolved geometric mean of  $0.^{\circ}64$  corresponding to an  $R_{90\%}$  radius of  $0.^{\circ}53$  that is  $\sim 1325$  au. As seen in Fig. 4, this shows that the emission from HDO (and thus likely of that of H<sub>2</sub>O in the gas phase) is comparable to that of the inner envelope, as well as that of methanol and methyl formate. Also formamide shows a similar, although

**Table 4.** Summary of the model results for the detected COMs.

| Position | Molecule                            | $C_{\text{vib}}^{(a)}$ | $N/N(\text{CH}_3\text{OH})$ | $N$<br>[cm $^{-2}$ ]   | $X^{(b)}$              | $T_{\text{rot}}$<br>[K] | $v_{\text{off}}^{(c)}$<br>[km s $^{-1}$ ] |
|----------|-------------------------------------|------------------------|-----------------------------|------------------------|------------------------|-------------------------|---|
| Shock-A  | CH <sub>3</sub> OH                  | 1                      | 1                           | $1.6 \times 10^{19}$   | $7.8 \times 10^{-6}$   | 180                     | -4.2                                      |
|          | CH <sub>3</sub> OCHO                | 1                      | 0.04                        | $6.4 \times 10^{17}$   | $3.1 \times 10^{-7}$   | 180                     | -4.2                                      |
|          | C <sub>2</sub> H <sub>5</sub> OH    | 1.44                   | 0.048                       | $7.7 \times 10^{17}$   | $3.8 \times 10^{-7}$   | 180                     | -4.2                                      |
|          | CH <sub>3</sub> COCH <sub>3</sub>   | 1                      | 0.025                       | $4.0 \times 10^{17}$   | $2.0 \times 10^{-7}$   | 180                     | -4.2                                      |
|          | a(CH <sub>2</sub> OH) <sub>2</sub>  | 1                      | 0.005                       | $8.0 \times 10^{16}$   | $3.9 \times 10^{-8}$   | 180                     | -4.2                                      |
|          | t-HCOOH <sup>(b)</sup>              | 1                      | 0.004                       | $6.4 \times 10^{16}$   | $3.1 \times 10^{-8}$   | 180                     | -4.2                                      |
|          | CH <sub>3</sub> CHO                 | 1                      | 0.002                       | $3.2 \times 10^{16}$   | $1.6 \times 10^{-8}$   | 180                     | -4.2                                      |
|          | CH <sub>3</sub> NCO                 | 1.03                   | 0.0041                      | $6.6 \times 10^{16}$   | $3.2 \times 10^{-8}$   | 180                     | -4.2                                      |
|          | C <sub>2</sub> H <sub>3</sub> CN    | 1                      | 0.0017                      | $2.7 \times 10^{16}$   | $1.3 \times 10^{-8}$   | 180                     | -4.2                                      |
|          | C <sub>2</sub> H <sub>5</sub> CN    | 1.7                    | 0.0057                      | $9.1 \times 10^{16}$   | $4.4 \times 10^{-8}$   | 180                     | -4.2                                      |
|          | HC(O)NH <sub>2</sub> <sup>(b)</sup> | 1.16                   | 0.0058                      | $9.3 \times 10^{16}$   | $4.6 \times 10^{-8}$   | 180                     | -4.2                                      |
|          | CH <sub>3</sub> OCH <sub>3</sub>    | 1                      | <0.1                        | < $1.6 \times 10^{18}$ | < $7.8 \times 10^{-7}$ | 180                     | -4.2                                      |
|          | HDO                                 | 1                      | 0.02                        | $3.2 \times 10^{17}$   | $1.6 \times 10^{-7}$   | 180                     | -4.2                                      |
| Shock-B  | CH <sub>3</sub> OH                  | 1                      | 1                           | $2.0 \times 10^{19}$   | $1.1 \times 10^{-5}$   | 180                     | +4.55                                     |
|          | CH <sub>3</sub> OCHO                | 1                      | 0.05                        | $1.0 \times 10^{18}$   | $5.3 \times 10^{-7}$   | 180                     | +4.55                                     |
|          | C <sub>2</sub> H <sub>5</sub> OH    | 1.44                   | 0.048                       | $9.6 \times 10^{17}$   | $5.1 \times 10^{-7}$   | 180                     | +4.55                                     |
|          | CH <sub>3</sub> COCH <sub>3</sub>   | 1                      | 0.025                       | $5.0 \times 10^{17}$   | $2.6 \times 10^{-7}$   | 180                     | +4.55                                     |
|          | a(CH <sub>2</sub> OH) <sub>2</sub>  | 1                      | 0.005                       | $1.0 \times 10^{17}$   | $5.3 \times 10^{-8}$   | 180                     | +4.55                                     |
|          | t-HCOOH <sup>(b)</sup>              | 1                      | 0.005                       | $1.0 \times 10^{17}$   | $5.3 \times 10^{-8}$   | 180                     | +4.55                                     |
|          | CH <sub>3</sub> CHO                 | 1                      | 0.002                       | $4.0 \times 10^{16}$   | $2.1 \times 10^{-8}$   | 180                     | +4.55                                     |
|          | CH <sub>3</sub> NCO                 | 1.03                   | 0.0041                      | $8.2 \times 10^{16}$   | $4.4 \times 10^{-8}$   | 180                     | +4.55                                     |
|          | C <sub>2</sub> H <sub>3</sub> CN    | 1                      | 0.0017                      | $3.3 \times 10^{16}$   | $1.8 \times 10^{-8}$   | 180                     | +4.55                                     |
|          | C <sub>2</sub> H <sub>5</sub> CN    | 1.7                    | 0.0049                      | $9.7 \times 10^{16}$   | $5.1 \times 10^{-8}$   | 180                     | +4.55                                     |
|          | HC(O)NH <sub>2</sub> <sup>(b)</sup> | 1.16                   | 0.0077                      | $1.6 \times 10^{17}$   | $8.2 \times 10^{-8}$   | 180                     | +4.55                                     |
|          | CH <sub>3</sub> OCH <sub>3</sub>    | 1                      | <0.1                        | < $2.0 \times 10^{18}$ | < $1.1 \times 10^{-6}$ | 180                     | +4.55                                     |
|          | HDO                                 | 1                      | 0.02                        | $4.0 \times 10^{17}$   | $2.1 \times 10^{-7}$   | 180                     | +4.55                                     |
| Envelope | CH <sub>3</sub> OH                  | 1                      | 1                           | $4.1 \times 10^{18}$   | $2.2 \times 10^{-6}$   | 110                     | +3.5                                      |
|          | CH <sub>3</sub> OCHO                | 1                      | 0.025                       | $1.03 \times 10^{17}$  | $5.4 \times 10^{-8}$   | 110                     | +3.5                                      |
|          | C <sub>2</sub> H <sub>5</sub> OH    | 1.1                    | 0.022                       | $9.0 \times 10^{16}$   | $4.7 \times 10^{-8}$   | 110                     | +3.5                                      |
|          | CH <sub>3</sub> COCH <sub>3</sub>   | 1                      | 0.01                        | $4.1 \times 10^{16}$   | $2.2 \times 10^{-8}$   | 110                     | +3.5                                      |
|          | a(CH <sub>2</sub> OH) <sub>2</sub>  | 1                      | 0.01                        | $4.1 \times 10^{16}$   | $2.2 \times 10^{-8}$   | 110                     | +3.5                                      |
|          | t-HCOOH <sup>(b)</sup>              | 1                      | 0.0033                      | $1.367 \times 10^{16}$ | $7.2 \times 10^{-9}$   | 110                     | +3.5                                      |
|          | CH <sub>3</sub> CHO                 | 1                      | 0.00167                     | $6.83 \times 10^{15}$  | $3.6 \times 10^{-9}$   | 110                     | +3.5                                      |
|          | CH <sub>3</sub> NCO                 | 1.0                    | 0.004                       | $1.64 \times 10^{16}$  | $8.6 \times 10^{-9}$   | 110                     | +3.5                                      |
|          | C <sub>2</sub> H <sub>3</sub> CN    | 1                      | 0.005                       | $2.05 \times 10^{16}$  | $1.1 \times 10^{-8}$   | 110                     | +3.5                                      |
|          | C <sub>2</sub> H <sub>5</sub> CN    | 1.18                   | 0.0118                      | $4.8 \times 10^{16}$   | $2.6 \times 10^{-8}$   | 110                     | +3.5                                      |
|          | HC(O)NH <sub>2</sub> <sup>(b)</sup> | 1.03                   | 0.01                        | $4.2 \times 10^{16}$   | $2.2 \times 10^{-8}$   | 110                     | +3.5                                      |
|          | CH <sub>3</sub> OCH <sub>3</sub>    | 1                      | <0.5                        | < $2.1 \times 10^{18}$ | < $1.1 \times 10^{-6}$ | 110                     | +3.5                                      |
|          | HDO                                 | 1                      | 0.05                        | $2.1 \times 10^{17}$   | $1.1 \times 10^{-7}$   | 110                     | +3.5                                      |

**Notes.** <sup>(a)</sup>Correction factor to the molecular column density to account for the contribution of torsionally or vibrationally excited states to the partition function. All parameters are calculated for the given  $T_{\text{kin}}$ . <sup>(b)</sup>The molecular abundance ( $X$ ) is calculated by  $X = N/N(\text{H}_2)$ . The values used for  $N(\text{H}_2)$  are given in Table 2. <sup>(c)</sup>Velocity offset compared to the  $v_{\text{lsr}}$  of -43.5 km s $^{-1}$ .

marginally smaller extent. Similarly to CH<sub>3</sub>OH and other O-bearing COMs, its peak is offset compared to the position of the protostar, suggesting that it has a higher abundance at the shock positions. This is confirmed by our modelling which measures the highest column density of HDO towards the B-shock position. In Fig. 5 we show the first moment map revealing the kinematics of the HDO emitting gas. The velocity pattern of HDO traced by its 1st moment map is very similar to that of CH<sub>3</sub>OH (Paper I), and is consistent with rotational motions with a velocity gradient roughly perpendicular to the outflow. This confirms that the bulk of observed HDO emission originates from the inner envelope.

## 4. Discussion

### 4.1. Shock chemistry instead of a radiatively heated envelope: precursor of a hot core

In Paper I we investigate the physical properties of the collapsing core and the protostellar envelope of G328.2551-0.5321, and estimate the current protostellar mass to be around  $16 M_{\odot}$  with an envelope mass of  $M_{\text{env}} \sim 120 M_{\odot}$ . Therefore, the protostar is very likely to form an O4-O5 type star with a final stellar mass of  $\sim 50 M_{\odot}$ . While the bulk of the CH<sub>3</sub>OH emission is extended over the inner envelope, at the close vicinity of the protostar, between

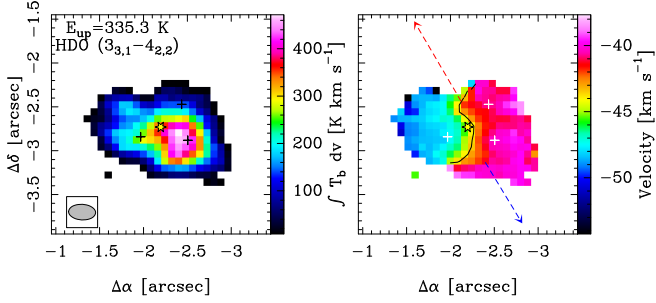


**Fig. 5.** Zeroth (left) and first (right) moment map of the HDO ( $J = 3_{3,1} - 4_{2,2}$ ) line calculated between  $-55$  and  $-35 \text{ km s}^{-1}$ . The yellow star marks the position of the dust continuum peak, and the black line shows the  $v_{\text{lsr}}$  at  $-43.5 \text{ km s}^{-1}$ . The red and blue arrows show the orientation of the outflow. The crosses mark the positions where the spectra were extracted for this study. The beam is shown in the lower left corner.

a projected distance of 300 and 800 au, a rotational transition from the vibrationally excited state of CH<sub>3</sub>OH at 334.436 GHz is interpreted as tracing shocks due to accretion. The accretion shocks imply the presence of an accretion disk, with a measured orientation perpendicular within  $10^\circ$  to the axis of the outflow. Since the accretion shocks on both the A and B positions are extended, we study here the molecular composition of positions that are the brightest in molecular emission along the extent of the accretion shocks (Fig. 1).

Our results on the overall molecular composition of the gas suggest a similar molecular richness compared to other high-mass star forming regions hosting classical, radiatively heated hot cores (Hatchell et al. 1998; Bisschop et al. 2007; Allen et al. 2017; Widicus Weaver et al. 2017). The COMs typical of hot cores are detected towards G328.2551-0.5321, however, several species are found to peak at the proposed accretion shocks rather than the radiatively heated core towards the protostar and the accretion disk. Inferred from CH<sub>3</sub>OH transitions, the bulk of the gas in the inner envelope is at a temperature of  $T_{\text{kin}} = 110 \text{ K}$  with a relatively small extent, a radius of  $\sim 1175 \text{ au}$ , and  $1450 \text{ au}$  for the most extended molecules, such as formamide and methyl formate, respectively (Sect. 3.3). This extent is comparable to the highest column density dust continuum emission detected with a 1500 au radius. Considering a spherically symmetric centrally illuminated core, the expected dust temperature is between 83 and 157 K at a radius of 1000 au for the protostellar luminosity of  $1.3 \times 10^4 L_\odot$  (Paper I) assuming radiative equilibrium (Goldreich & Kwan 1974; Wolfire & Cassinelli 1986; Wilner et al. 1995). This is broadly consistent with the temperature estimate from the molecular line emission for the bulk of the inner envelope. However, instead of a gradual warming up of the gas due to the radiative heating of the protostar, we identify localised spots of heated gas towards the accretion shocks with  $T_{\text{kin}} = 180 \text{ K}$ .

Since the source hosts a deeply embedded protostar, a radiatively heated inner core is expected towards the central position. The most compact emission peaking on the protostar is traced by vinyl and ethyl cyanides and has a radius of 900 au along its minor axis. Assuming that molecules with a CN group outline the largest potential extent of a radiatively heated inner core implies that this region must be very compact. Massive protostars or YSOs observed towards well studied high-mass star forming regions exhibit a considerably more extended heated inner region. For example Ginsburg et al. (2017) resolve the region with high gas temperatures of  $T > 100 \text{ K}$  out to 5000 au towards the hot cores of the W51 Main star forming region, and

Bonfand et al. (2017) measure an extent of  $\sim 3000 \text{ au}$  towards compact hot cores in the SgrB2 star forming region. Other hot cores typically have an even larger extent of warm gas up to  $0.1 \text{ pc}$  (Hatchell et al. 1998; Kurtz et al. 2000; Cesaroni 2005). In this context the current state of G328.2551-0.5321 is likely to represent an earlier evolutionary stage compared to classical hot cores, and where localised spots of heated gas due to accretion shocks, hence a different heating mechanism leaves an observable imprint on the physical and chemical properties of the gas, since the highest column densities of COMs originate from the accretion shocks.

In the case of G328.2551-0.5321, based on the radiative equilibrium model, a  $\sim 15 \times$  higher protostellar luminosity would be required to heat the dust to  $T > 100 \text{ K}$  at a 5000 au radius. Given the large expected final stellar mass of  $M_\star \sim 50 M_\odot$  of the protostar in G328.2551-0.5321, it is very likely that the radiatively heated region is going to expand, turning this object into a classical radiatively heated hot core with a comparably large extent of heated gas as other known objects.

In addition to these physical arguments, the molecular composition could also be used to obtain an age estimate of the gas (e.g. Viti et al. 2004; Caselli et al. 1993; Garrod et al. 2008; Allen et al. 2018). Overall, we detect several molecules that are suggested to be “first generation” COMs originating from grain surface chemistry, based on the observational study of Bisschop et al. (2007), such as CH<sub>3</sub>OH, C<sub>2</sub>H<sub>5</sub>OH, CH<sub>3</sub>OCHO, HC(O)NH<sub>2</sub>, CH<sub>3</sub>CN, and C<sub>2</sub>H<sub>5</sub>CN, although the spatial distribution of these molecules is resolved and shows significant differences (see Sect. 4.3). Chemical age estimates for hot cores have been based on molecular richness (Calcutt et al. 2014), ratios of chemically related species such as C<sub>2</sub>H<sub>3</sub>CN and C<sub>2</sub>H<sub>5</sub>CN (e.g. Fontani et al. 2007; Zeng et al. 2018; Allen et al. 2018), and dedicated physico-chemical modelling of hot cores (Bonfand et al. 2019). The observed ratio of C<sub>2</sub>H<sub>3</sub>CN and C<sub>2</sub>H<sub>5</sub>CN towards G328.2551-0.5321 is consistent with a source that is still chemically young according to the chemical models by Caselli et al. (1993), although Charnley et al. (1992) and Rodgers & Charnley (2001) suggest that additional C<sub>2</sub>H<sub>3</sub>CN may form in gas phase reactions compared to those models. In this context the overall chemical composition of G328.2551-0.5321 resembles that of a young hot core with an age  $< 10^5 \text{ yr}$ , and is different from sources where chemistry is driven by low velocity shocks and a high cosmic ray flux (Zeng et al. 2018). Recent models by Allen et al. (2018), for example, reproduce the observed abundances of cyanides using a short warm-up phase, however, including a higher cosmic ionisation rate towards one hot core in their sample was necessary. Therefore, it remains unclear how reliable such age estimates can be, missing gas-phase reactions for the production of cyanides as well as variations in physical conditions may impact age estimates.

#### 4.2. Chemical differentiation at the innermost 1500 au scales of the protostar: the O/N dichotomy

One of the most striking results of our analysis is the observed spatial dichotomy between O- and N-bearing COMs on scales smaller than  $\sim 1000 \text{ au}$  observed towards the inner envelope. While the O-bearing COMs are associated with the inner envelope and the shock spots, the N-bearing COMs are located in the immediate vicinity of the protostar and the accretion disk and show an extension in the direction of the outflow. Only formamide shows a more extended distribution, similar to that of methyl formate.

Chemical differentiation, a.o., the O/N dichotomy, has been first observed on larger scales towards Orion-KL (Caselli et al. 1993) as well as W3(OH) and W3(H<sub>2</sub>O) (Wyrowski et al. 1999) originating from different physical components within these star forming regions. On scales smaller than 3000 au this has been further confirmed towards Orion-KL (Blake et al. 1996; Wright et al. 1996; Widicus Weaver & Friedel 2012; Friedel & Widicus Weaver 2012; Feng et al. 2015), as well as other high-mass star forming cores, such as G10.61–0.23 (Qin et al. 2010) followed by several other examples, like AFGL2591 (Jiménez-Serra et al. 2012), NGC7538IRS9 (Öberg et al. 2013), G35.20, G35.03 (Allen et al. 2017), and other sources like more evolved MYSOs (Fayolle et al. 2015). G328.2551-0.5321 is, however, the first example where we can study such a chemical differentiation in a single, well resolved collapsing envelope, and associate the observed molecules to their physical origin within the envelope. This makes this source a favourable target to study the origin of chemical differentiation as well as the emergence, and chemical evolution of hot cores.

From the O-bearing COMs except methanol, methyl formate has the largest column density, and its distribution resembles that of the low-excitation CH<sub>3</sub>OH lines shown in more detail in Paper I. This is, however, not surprising, since methyl formate is chemically related to methanol (Garrod & Herbst 2006). The observed spatial distribution and its presence in a moderately warm gas phase may suggest grain surface production and subsequent sublimation to the gas phase. Dimethyl ether, a chemically related molecule to methyl formate remains, however, undetected up to a relative fraction of 10–50% compared to methanol towards both the shock and the envelope positions, despite having transitions in a range of upper energy levels similar to that of methyl formate. The models of Garrod & Herbst (2006) predict a ratio between the gas phase fractional abundances of methyl formate and dimethyl ether between 0.24 and 17 at different times of their models, while observations suggest a molecular abundance of the same order of magnitude for both species (Garrod & Herbst 2006; Cazaux et al. 2003; Taquet et al. 2015). Our sensitivity is, however, not sufficient to detect dimethyl ether at a similar column density compared to methyl formate.

While methyl formate is abundant over the entire extent of the inner envelope, the lowest column density O-bearing COMs, such as ethanol and ethylene glycol are only detected towards the accretion shocks first recognised by the torsionally excited state CH<sub>3</sub>OH line in Paper I. The distribution of these primarily O-bearing COMs is rather similar to the high excitation methanol emission showing two peaks offset from the dust continuum and thus the central protostar (Fig. 4). Similarly to the high excitation methanol lines, their velocity pattern shows the two velocity components offset by  $\sim\pm4.5\text{ km s}^{-1}$  with respect to the  $v_{\text{lsr}}$  of the source. This allows us to conclude that due to the change of physical conditions at the accretion shocks, heavier O-bearing COMs outline well the existence of these shocks.

The N-bearing COMs, especially vinyl and ethyl cyanides, are located towards the immediate vicinity of the protostar and the accretion disk and show an extension in the direction of the outflow. This suggests that they are also associated with the innermost region of the outflow cavity, and potentially the accretion disk as also suggested for the vibrationally excited,  $v_7 = 1$  state HC<sub>3</sub>N transition at 346.456 GHz in Paper I. Our results provide the first direct evidence that, in contrast to O-bearing COMs, molecules with a CN group peak on the innermost few hundred au vicinity of the protostar likely associated with regions of hot gas, which explains why some studies may find

them at elevated temperatures relative to the O-bearing COMs (Qin et al. 2010; Widicus Weaver et al. 2017).

In fact models of photodissociation regions (PDRs) show that the CN emission is sensitive to the UV radiation (e.g. Jansen et al. 1995; Sternberg & Dalgarno 1995; van Zadelhoff et al. 2003; Walsh et al. 2010), which could explain the enhancement of molecules with a CN group towards the central position associated with the accretion disk. For example, towards low-mass embedded protostars CN has been proposed to trace the outflow cavity walls (Jørgensen 2004), while CN is also one of the brightest tracers of protoplanetary disks (Guilloteau et al. 2014; Cazzoletti et al. 2018), where it has been proposed to trace the UV impacted upper warm molecular layers.

As for hot cores, complex cyanides have been modelled by Allen et al. (2018), who suggest that a longer warm up time together with a higher cosmic ray ionisation rate is necessary to reproduce the observed high abundance of vinyl and ethyl cyanides. The chemical differentiation between O- and N-bearing COMs observed toward the Orion Hot Core and Compact Ridge could also be explained with a different thermal evaporation history (Caselli et al. 1993).

The case of formamide is somewhat in between these two components, as this molecule shows strong emission towards the dust peak while it is also present in the inner envelope, and shows brighter emission towards at least one of the shock positions. The observed difference compared to the other N-bearing COMs may be explained by a different chemical formation pathway due to its amide bond ( $-\text{N}-\text{C}(=\text{O})-$ ), which is also suggested by the fact that it has been detected in various environments, such as low-mass protostars (López-Sepulcre et al. 2015), also showing a ring around the central object (Coutens et al. 2016); hot cores (Bisschop et al. 2007); and shocks (Mendoza et al. 2014). Although we find a spatial correlation between methanol, methyl formate and formamide, this does not provide enough constraints on the chemical formation routes, that is a grain surface production and sublimation versus gas-phase formation scenario. Therefore, the formation pathway of formamide remains unclear (cf. Mendoza et al. 2014), in addition to the gas-phase reactions, its grain surface production could be efficient (Garrod et al. 2008).

#### 4.3. Change of molecular composition at the accretion shocks

Based on the molecular emission and the kinetic temperatures ( $T_{\text{kin}}$ ) derived from our LTE modelling, towards G328.2551-0.5321 we identify three distinct physical components hosting emission of COMs: (1) the inner envelope showing extended emission of methyl formate, HDO and formamide with  $T_{\text{kin}} = 110\text{ K}$  and an extent of  $\sim 1000\text{--}1500\text{ au } FWHM$ ; (2) the shock spots with a higher kinetic temperature of  $T_{\text{kin}} = 160\text{--}190\text{ K}$  together with an enhanced column density of O-bearing COMs. Ethanol, acetone, and ethylene glycol show, for example, the highest column density and abundance towards the shock positions. The kinematics of these species further confirms their association with the accretion shocks as they show prominently the two velocity components with  $\sim\pm4.5\text{ km s}^{-1}$  offset from the source  $v_{\text{lsr}}$ , similarly as the CH<sub>3</sub>OH  $v_t = 1$  line reported in Paper I; (3) the closest vicinity of the protostar and its accretion disk characterised by N-bearing COMs with a CN group, such as vinyl and ethyl cyanide.

Since blending and dust opacity hinders us from a quantitative analysis of the molecular composition towards the central position, here we compare the molecular abundances between

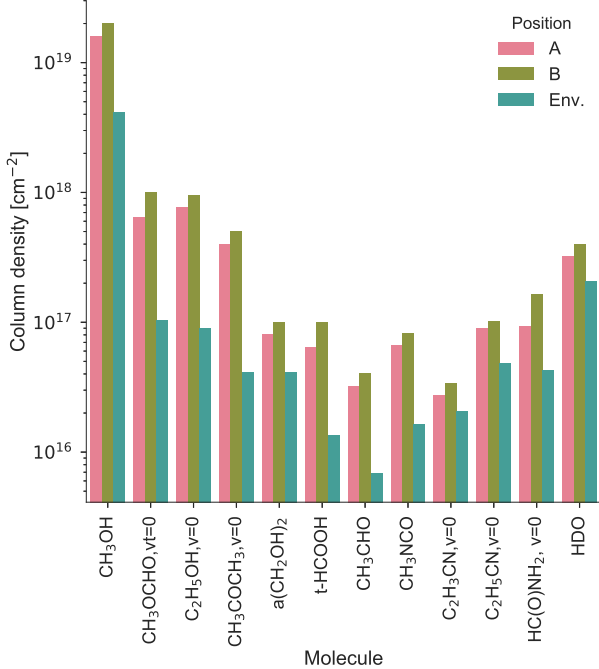


**Fig. 6.** Molecular column densities obtained from the Weeds LTE modelling of COMs and HDO. The three positions (shock-*A*, -*B* and the position toward the inner envelope) are labelled in different colours.

the accretion shocks and the inner envelope. Towards the shock positions we estimate a beam averaged H<sub>2</sub> column density,  $N(\text{H}_2)$ , of  $1.89\text{--}2.04 \times 10^{24} \text{ cm}^{-2}$  assuming a dust temperature,  $T_d = T_{\text{kin}}$  of 180 K. In contrast, towards the inner envelope we measure a somewhat lower kinetic temperature of 110 K and  $N(\text{H}_2) = 1.9 \times 10^{24} \text{ cm}^{-2}$ . This suggests that considering the temperature variations, the H<sub>2</sub> column densities at the three positions are practically identical. Our modelling shows that the abundance of CH<sub>3</sub>OH reaches up to  $7.8 \times 10^{-6}\text{--}1.1 \times 10^{-5}$  towards the accretion shocks, it is, however, up to a factor of five lower towards the inner envelope with an abundance of  $2.2 \times 10^{-6}$ . The other O-bearing COMs have a molecular abundance relative to H<sub>2</sub> between  $1.6 \times 10^{-8}$  and  $5.3 \times 10^{-7}$  towards the shock positions, and an order of magnitude lower abundance range, between  $3.6 \times 10^{-9}$  and  $5.4 \times 10^{-8}$  towards the position representing the bulk of the inner envelope. Compared to the most abundant O-bearing COMs, such as methyl formate, the N-bearing COMs like vinyl and ethyl cyanide have up to an order of magnitude lower abundance range, between  $1.3 \times 10^{-8}$  and  $5.1 \times 10^{-8}$  towards the shock positions. The estimated abundances are also lower towards the inner envelope, and range between  $8.6 \times 10^{-9}$  and  $2.6 \times 10^{-8}$  for all the N-bearing COMs. The molecular abundances of formamide are of the order of  $10^{-8}$ , at least one order of magnitude higher than observed towards hot corino objects (López-Sepulcre et al. 2015), although our estimations are only based on practically one transition and may not be robust for this molecule. The estimated molecular abundances are listed in Table 4.

We compare the molecular composition towards the shock positions and the inner envelope in Fig. 6. In general, we find that the molecular composition of the two shock spots are broadly consistent with each other, and show very similar molecular abundances for most species. However, the observed molecular abundance of COMs with respect to H<sub>2</sub> towards the inner envelope is found to be several factors lower compared to the

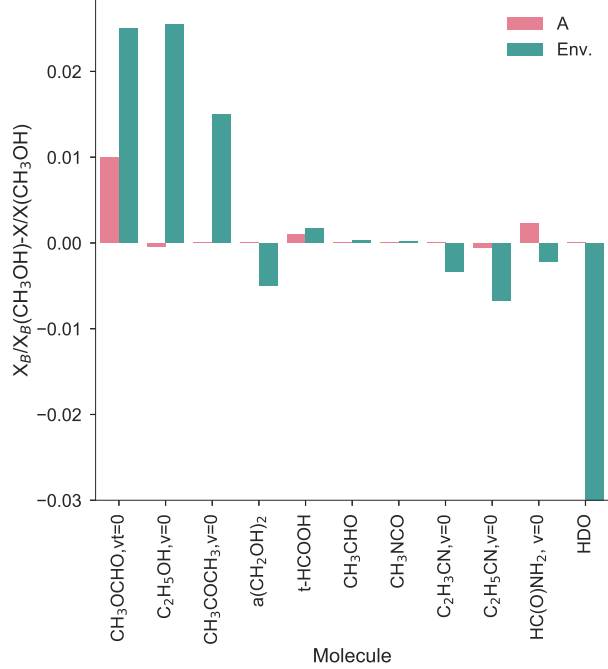


**Fig. 7.** Relative molecular abundances with respect to that of the *B*-shock position. Positive means a relative decrease of certain species compared to the same molecular abundance derived at the *B*-shock position.

shock spots. After methanol, methyl formate is the second most abundant molecule both in the shock spots and in the envelope. Towards the position of the inner envelope, it shows, however, a much higher relative abundance relative to CH<sub>3</sub>OH.

The change of molecular abundances normalised to CH<sub>3</sub>OH with respect to the *B* shock position is shown in Fig. 7. This further suggests that the relative change of molecular composition between the *A* and *B* shock spots is small, thus their molecular composition is similar. The molecular composition towards the inner envelope is, however, considerably different, in particular the relative fraction to CH<sub>3</sub>OH from methyl formate, ethanol and acetone is smaller in the inner envelope than at the *B* shock position, suggesting that the gas becomes enriched in these O-bearing COMs in the shocks.

HDO has a similar abundance towards the inner envelope and the accretion shocks, suggesting that not only the accretion shocks but also the inner envelope has a significant contribution to the overall amount of HDO. Its relative fraction compared to methanol changes, however, significantly and becomes considerably higher towards the inner envelope. This is simply because the methanol abundance is lower towards the inner envelope compared to the accretion shocks.

In contrast, the cyanides show a relatively moderate change of abundance ratio between the envelope and the accretion shocks. The C<sub>2</sub>H<sub>5</sub>CN/C<sub>2</sub>H<sub>3</sub>CN abundance ratio is 2.4–3.4 towards all positions, suggesting that saturated nitriles are in general more abundant than unsaturated ones, which is expected for hot cores. Saturated molecules are chemically more stable which may explain their observed higher abundance. Chemical models predict that (e.g. Caselli et al. 1993) C<sub>2</sub>H<sub>3</sub>CN forms from C<sub>2</sub>H<sub>5</sub>CN through ion-molecule reactions in the gas phase, therefore their ratio has been suggested as a tracer for the chemical age of hot cores. For example Fontani et al. (2007) find C<sub>2</sub>H<sub>5</sub>CN/C<sub>2</sub>H<sub>3</sub>CN abundance ratios around 2.0–3.3 towards six classical hot cores and conclude that their age is less

than  $10^5$  yr. Such a ratio is also consistent with that found towards Orion-KL and SgrB2(N) (Zeng et al. 2018), however towards SgrB2(N) high angular resolution measurements resolving the individual hot cores suggest very different ratios and find  $C_2H_5CN/C_2H_3CN = 5-17$ . The evolutionary sequence towards SgrB2(N) based on the  $C_2H_5CN/C_2H_3CN$  ratio is, however, contradicting the results of dedicated physico-chemical modelling (Bonfand et al. 2019) suggesting that either the chemical network lacks some reactions or that other physical parameters such as the stellar mass and ionisation rate may have a stronger impact on the chemical evolution than the age.

Altogether this quantitatively demonstrates a change in the molecular composition of COMs between the envelope and the accretion shocks, while Fig. 4 shows that also the central position is likely to have an even more drastic change of molecular composition. The origin of this different chemistry observed towards the central position, the accretion shocks and the inner envelope needs to be understood. As discussed earlier, the chemistry of N-bearing COMs with a CN group may be influenced by a strong change of physical conditions in the immediate vicinity of the protostar, such as UV radiation as well as the gas being exposed to a heating source for a longer time-scale compared to the gas within the cold envelope. A different thermal history of the gas, together with different initial conditions for the chemistry in the envelope due to thermal or non-thermal desorption processes could be responsible for the observed spatial segregation of molecules.

#### 4.4. Distribution of deuterated water

HDO from cold and hot gas has been detected towards classical hot cores both at low and high angular resolution (e.g. Jacq et al. 1990; van der Tak et al. 2006; Liu et al. 2013). Here we resolve for the first time HDO emission towards the inner regions of a high-mass protostellar envelope and find that it is associated with the inner envelope. Its velocity field is axisymmetric roughly perpendicular to the outflow direction consistent with a rotational pattern also observed in several  $CH_3OH$  transitions. A similar rotational pattern has also been observed towards AFGL 2591, where, based on its correlation with the continuum structure, it has been proposed to trace a circumstellar disk (van der Tak et al. 2006). In addition, HDO shows an enhanced molecular column density towards at least one of the shock positions, and similarly to the O-bearing COMs, its emission does not show a prominent peak on the position of the protostar.

Since we only have one observed transition, the estimated parameters of HDO rely on the assumption that the emitting gas has the same rotational temperature as  $CH_3OH$ , which is 180 K for the shock position and 110 K on the position of the inner envelope. This gives an estimate of the HDO column density of 2.1 and  $4.0 \times 10^{17} \text{ cm}^{-2}$  towards the inner envelope and the shock position, respectively. The HDO column density is relatively similar towards the shock spots and the inner envelope, however its relative fraction compared to  $CH_3OH$  is higher in the envelope than in the accretion shocks by a factor of 2. As a comparison, towards G34.26+0.15, one of the classical hot cores, Coutens et al. (2014) estimate an HDO column density of  $\sim 1.6 \times 10^{16} \text{ cm}^{-2}$  with an excitation temperature of  $\sim 79$  K towards the inner regions of the hot core. Our estimates give an HDO abundance of  $X(HDO) = 1.1-2.1 \times 10^{-7}$  relative to  $H_2$ , which is of the same order of magnitude as Liu et al. (2011) find for the  $T > 100$  K regime for G34.26+0.15, and what Kulczak-Jastrzebska (2017) estimates for the inner region of other classical hot cores.

The kinetic temperature of the inner envelope is mainly estimated based on methanol and methyl formate, and because HDO shows a similar spatial distribution to these species, it is reasonable to assume that it is also associated with gas close to, or just above the ice sublimation temperature,  $T = 90-190$  K. This would suggest that the observed HDO emission likely originates from the evaporation of the grain surfaces, expected at  $\gtrsim 100$  K, (Fraser et al. 2001). This is also consistent with the abundance jump assumed by modelling of single dish (low resolution) observations for classical hot cores, as well as low- to intermediate mass Class 0 protostars (Comito et al. 2003; Parise et al. 2005; Liu et al. 2013).

Our detection of HDO from the inner envelope is intriguing, because chemical models predict a decrease in the abundance of water, and therefore HDO towards the inner 1000 au of hot cores (Coutens et al. 2014), with the destruction of HDO being even more efficient than the destruction of  $H_2O$ . In comparison to our results, both the location and the relatively high abundance of HDO suggest that  $H_2O$ , and HDO destruction has not been efficient in this source yet, providing further evidence that the source is chemically young.

## 5. Conclusions

Using high angular-resolution observations with ALMA, we investigate the physical and chemical structure of the massive envelope of a high-mass protostar, G328.2551-0.5321. We identify emission from 10 COMs using LTE modelling of a 7.5 GHz non continuous spectral coverage around 345 GHz, and find that its overall molecular composition shows a similar richness compared to other high-mass star forming regions.

Comparing to recent observations of hot cores, the radiatively heated inner region is the most compact observed to date with a radius ( $R_{90\%}$ ) of  $< 900$  au estimated from vinyl and ethyl cyanides. Inferred from  $CH_3OH$  transitions, the bulk of the gas in the inner envelope is at a temperature of  $T_{kin} = 110$  K, allowing us to witness the emergence of accretion shocks suggesting a different heating mechanism compared to the classical, radiatively heated hot cores. However, given the  $\sim 50 M_\odot$  expected final stellar mass, G328.2551-0.5321 is likely to represent an earlier evolutionary stage compared to classical hot cores.

For the first time, we spatially resolve on  $< 1000$  au scales within a single collapsing envelope the chemical differentiation of O-bearing COMs versus N-bearing COMs, in particular those with a CN group. The O-bearing COMs, such as ethanol, acetone, ethylene glycol and acetaldehyde have an increased abundance towards the two localised positions of accretion shocks with  $T_{kin} = 180$  K. These transitions show the same velocity pattern as the  $CH_3OH v_t = 1$  emission at 334.436 GHz reported in Paper I, representing the accretion shocks. Emission from other COMs, such as methanol, methyl formate, and formamide is found towards an extended region with a radius ( $R_{90\%}$ ) of 1175–1450 au and  $T_{kin} = 110$  K.

We image and spatially resolve emission from the HDO ( $J = 3_{3,1}-4_{2,2}$ ) line. It is extended over the inner envelope and its velocity pattern is consistent with a velocity gradient roughly perpendicular to the outflow, likely corresponding to the rotational pattern of the inner envelope. Its extent is comparable to that of methyl formate with  $T_{kin} = 110$  K. The high HDO column density suggests that the destruction of water has not been efficient towards this source since HDO is expected to be destroyed in the inner regions of classical hot cores.

We identify three physical components within the envelope, a compact inner region representing the immediate vicinity of the

protostar and its accretion disk, the inner envelope, and the accretion shocks within the envelope. We quantitatively show that the molecular composition of COMs towards the two accretion shocks is similar, while there is a change of molecular composition among COMs compared to the inner envelope. In addition, we qualitatively show that the central regions are particularly apparent in N-bearing COMs with a CN group, such as vinyl and ethyl cyanide that could explain the typically observed higher temperatures found with these molecules towards classical hot cores.

**Acknowledgements.** This paper makes use of the ALMA data: ADS/JAO.ALMA 2013.1.00960.S. ALMA is a partnership of ESO (representing its member states), NSF (USA), and NINS (Japan), together with NRC (Canada), NSC and ASIAA (Taiwan), and KASI (Republic of Korea), in cooperation with the Republic of Chile. The Joint ALMA Observatory is operated by ESO, AUI/NRAO, and NAOJ. T.Cs. acknowledges support from the Deutsche Forschungsgemeinschaft, DFG via the SPP (priority programme) 1573 “Physics of the ISM”.

## References

- Allen, V., van der Tak, F. F. S., Sánchez-Monge, Á., Cesaroni, R., & Beltrán, M. T. 2017, [A&A](#), **603**, A133
- Allen, V., van der Tak, F. F. S., & Walsh, C. 2018, [A&A](#), **616**, A67
- Balucani, N., Ceccarelli, C., & Taquet, V. 2015, [MNRAS](#), **449**, L16
- Beltrán, M. T., Codella, C., Viti, S., Neri, R., & Cesaroni, R. 2009, [ApJ](#), **690**, L93
- Bisschop, S. E., Jørgensen, J. K., van Dishoeck, E. F., & de Wachter, E. B. M. 2007, [A&A](#), **465**, 913
- Blake, G. A., Sutton, E. C., Masson, C. R., & Phillips, T. G. 1987, [ApJ](#), **315**, 621
- Blake, G. A., Mundy, L. G., Carlstrom, J. E., et al. 1996, [ApJ](#), **472**, L49
- Bonfand, M., Belloche, A., Menten, K. M., Garrod, R. T., & Müller, H. S. P. 2017, [A&A](#), **604**, A60
- Bonfand, M., Belloche, A., Garrod, R. T., et al. 2019, [A&A](#), **628**, A27
- Brouillet, N., Despois, D., Baudry, A., et al. 2013, [A&A](#), **550**, A46
- Calcutt, H., Viti, S., Codella, C., et al. 2014, [MNRAS](#), **443**, 3157
- Caselli, P., Hasegawa, T. I., & Herbst, E. 1993, [ApJ](#), **408**, 548
- Cazaux, S., Tielens, A. G. G. M., Ceccarelli, C., et al. 2003, [ApJ](#), **593**, L51
- Cazzoletti, P., van Dishoeck, E. F., Visser, R., Facchini, S., & Bruderer, S. 2018, [A&A](#), **609**, A93
- Cesaroni, R. 2005, [Ap&SS](#), **295**, 5
- Charnley, S. B. 2001, [ApJ](#), **562**, L99
- Charnley, S. B., Tielens, A. G. G. M., & Millar, T. J. 1992, [ApJ](#), **399**, L71
- Churchwell, E. 2002, [ARA&A](#), **40**, 27
- Comito, C., Schilke, P., Gerin, M., et al. 2003, [A&A](#), **402**, 635
- Coutens, A., Vastel, C., Hincelin, U., et al. 2014, [MNRAS](#), **445**, 1299
- Coutens, A., Jørgensen, J. K., van der Wiel, M. H. D., et al. 2016, [A&A](#), **590**, L6
- Csengeri, T., Urquhart, J. S., Schuller, F., et al. 2014, [A&A](#), **565**, A75
- Csengeri, T., Bontemps, S., Wyrowski, F., et al. 2017, [A&A](#), **601**, A60
- Csengeri, T., Bontemps, S., Wyrowski, F., et al. 2018, [A&A](#), **617**, A89
- Endres, C. P., Schlemmer, S., Schilke, P., Stutzki, J., & Müller, H. S. P. 2016, [J. Mol. Spectr.](#), **327**, 95
- Fayolle, E. C., Öberg, K. I., Garrod, R. T., van Dishoeck, E. F., & Bisschop, S. E. 2015, [A&A](#), **576**, A45
- Feng, S., Beuther, H., Henning, T., et al. 2015, [A&A](#), **581**, A71
- Fontani, F., Pasucci, I., Caselli, P., et al. 2007, [A&A](#), **470**, 639
- Fraser, H. J., Collings, M. P., McCoustra, M. R. S., & Williams, D. A. 2001, [MNRAS](#), **327**, 1165
- Friedel, D. N., & Widicus Weaver, S. L. 2012, [ApJS](#), **201**, 17
- Garay, G., & Lizano, S. 1999, [PASP](#), **111**, 1049
- Garrod, R. T., & Herbst, E. 2006, [A&A](#), **457**, 927
- Garrod, R. T., & Widicus Weaver, S. L. 2013, [Chem. Rev.](#), **113**, 8939
- Garrod, R. T., Widicus Weaver, S. L., & Herbst, E. 2008, [ApJ](#), **682**, 283
- Ginsburg, A., Goddi, C., Kruijssen, J. M. D., et al. 2017, [ApJ](#), **842**, 92
- Goldreich, P., & Kwan, J. 1974, [ApJ](#), **189**, 441
- Guilloteau, S., Simon, M., Piétu, V., et al. 2014, [A&A](#), **567**, A117
- Hatchell, J., Thompson, M. A., Millar, T. J., & MacDonald, G. H. 1998, [A&AS](#), **133**, 29
- Herbst, E., & van Dishoeck, E. F. 2009, [ARA&A](#), **47**, 427
- Jaber, A. A., Ceccarelli, C., Kahane, C., & Caux, E. 2014, [ApJ](#), **791**, 29
- Jacq, T., Walmsley, C. M., Henkel, C., et al. 1990, [A&A](#), **228**, 447
- Jansen, D. J., Spaans, M., Hogerheijde, M. R., & van Dishoeck, E. F. 1995, [A&A](#), **303**, 541
- Jiménez-Serra, I., Zhang, Q., Viti, S., Martín-Pintado, J., & de Wit, W.-J. 2012, [ApJ](#), **753**, 34
- Jørgensen, J. K. 2004, [A&A](#), **424**, 589
- Kulczak-Jastrzębska, M. 2017, [ApJ](#), **835**, 121
- Kurtz, S., Cesaroni, R., Churchwell, E., Hofner, P., & Walmsley, C. M. 2000, [Protostars and Planets IV](#) (Tucson, AZ: University of Arizona Press), 299
- Liu, F.-C., Parise, B., Kristensen, L., et al. 2011, [A&A](#), **527**, A19
- Liu, F.-C., Parise, B., Wyrowski, F., Zhang, Q., & Güsten, R. 2013, [A&A](#), **550**, A37
- López-Sepulcre, A., Jaber, A. A., Mendoza, E., et al. 2015, [MNRAS](#), **449**, 2438
- Maret, S., Hily-Blant, P., Pety, J., Bardeau, S., & Reynier, E. 2011, [A&A](#), **526**, A47
- Maud, L. T., Hoare, M. G., Galván-Madrid, R., et al. 2017, [MNRAS](#), **467**, L120
- Mendoza, E., Lefloch, B., López-Sepulcre, A., et al. 2014, [MNRAS](#), **445**, 151
- Millar, T. J., Herbst, E., & Charnley, S. B. 1991, [ApJ](#), **369**, 147
- Mookerjea, B., Casper, E., Mundy, L. G., & Looney, L. W. 2007, [ApJ](#), **659**, 447
- Müller, H. S. P., Schlöder, F., Stutzki, J., & Winnewisser, G. 2005, [J. Mol. Struct.](#), **742**, 215
- Öberg, K. I., Boamah, M. D., Fayolle, E. C., et al. 2013, [ApJ](#), **771**, 95
- Ordu, M. H., Zingsheim, O., Belloche, A., et al. 2019, [A&A](#), **629**, A72
- Ossenkopf, V., & Henning, T. 1994, [A&A](#), **291**, 943
- Oya, Y., Sakai, N., Watanabe, Y., et al. 2017, [ApJ](#), **837**, 174
- Palau, A., Fuente, A., Girart, J. M., et al. 2011, [ApJ](#), **743**, L32
- Palau, A., Walsh, C., Sánchez-Monge, Á., et al. 2017, [MNRAS](#), **467**, 2723
- Parise, B., Caux, E., Castets, A., et al. 2005, [A&A](#), **431**, 547
- Pickett, H. M., Poynter, R. L., Cohen, E. A., et al. 1998, [J. Quant. Spectr. Rad. Transf.](#), **60**, 883
- Qin, S.-L., Wu, Y., Huang, M., et al. 2010, [ApJ](#), **711**, 399
- Rodgers, S. D., & Charnley, S. B. 2001, [ApJ](#), **546**, 324
- Sakai, N., Sakai, T., Hirota, T., et al. 2014, [Nature](#), **507**, 78
- Sánchez-Monge, Á., Cesaroni, R., Beltrán, M. T., et al. 2013, [A&A](#), **552**, L10
- Sánchez-Monge, Á., Schilke, P., Schmiedekne, A., et al. 2017, [A&A](#), **604**, A6
- Schuller, F., Menten, K. M., Contreras, Y., et al. 2009, [A&A](#), **504**, 415
- Sternberg, A., & Dalgarno, A. 1995, [ApJS](#), **99**, 565
- Taquet, V., López-Sepulcre, A., Ceccarelli, C., et al. 2015, [ApJ](#), **804**, 81
- van der Tak, F. F. S., Walmsley, C. M., Herpin, F., & Ceccarelli, C. 2006, [A&A](#), **447**, 1011
- van Zadelhoff, G.-J., Aikawa, Y., Hogerheijde, M. R., & van Dishoeck, E. F. 2003, [A&A](#), **397**, 789
- Viti, S., Collings, M. P., Dever, J. W., McCoustra, M. R. S., & Williams, D. A. 2004, [MNRAS](#), **354**, 1141
- Walmsley, C. M., & Schilke, P. 1993, [Dust and Chemistry in Astronomy](#), eds. T. J. Millar, & D. A. Williams (Boca Raton: CRC Press), 37
- Walsh, C., Millar, T. J., & Nomura, H. 2010, [ApJ](#), **722**, 1607
- Widicus Weaver, S. L., & Friedel, D. N. 2012, [ApJS](#), **201**, 16
- Widicus Weaver, S. L., Laas, J. C., Zou, L., et al. 2017, [ApJS](#), **232**, 3
- Wilner, D. J., Welch, W. J., & Forster, J. R. 1995, [ApJ](#), **449**, L73
- Wolfire, M. G., & Cassinelli, J. P. 1986, [ApJ](#), **310**, 207
- Wright, M. C. H., Plambeck, R. L., & Wilner, D. J. 1996, [ApJ](#), **469**, 216
- Wyrowski, F., Schilke, P., Walmsley, C. M., & Menten, K. M. 1999, [ApJ](#), **514**, L43
- Zeng, S., Jiménez-Serra, I., Rivilla, V. M., et al. 2018, [MNRAS](#), **478**, 2962

## **Appendix A: Spectra obtained towards the A-shock position, and the inner envelope**



**Fig. A.1.** Same as Fig. 3 extracted towards the A-shock position.



**Fig. A.2.** Same as Fig. 3 extracted towards a position of the inner envelope.